Department of Precision and Microsystems Engineering

Study and improvement of dynamics of an Electron Beam Lithography Machine

Akash Kumar Jain

Report no	:	2021.045
Coach/ Professor	:	Dr. Ir. H. HosseinNia
Specialisation	:	Mechatronics System Design
Type of report	:	MSc Thesis
Date	:	21 July 2021

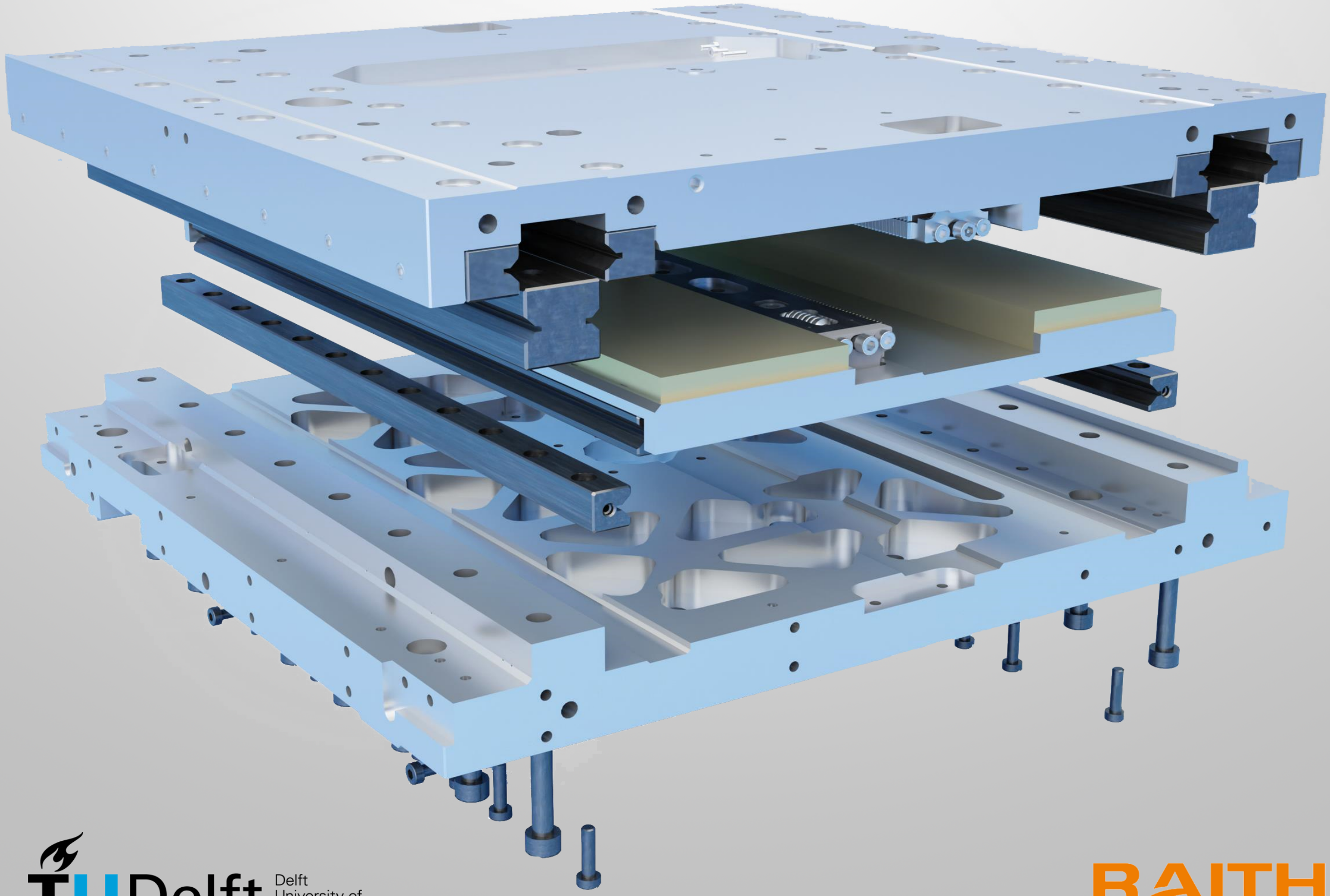

Challenge the future

Study and improvement of dynamics of an Electron Beam Lithography Machine

by

Akash Kumar Jain

to obtain the degree of
Master of Science in Mechanical Engineering
at the Delft University of Technology,
to be defended publicly on Wednesday July 21, 2021 at 02:30 PM.

Student number:	5072336	
Project duration:	August 17, 2020 – June 30, 2021	
Thesis committee:	Dr. Ir. H. HosseinNia,	TU Delft, supervisor
	Ir. J. W. Spronck,	TU Delft
	Dr. Ir. R. Saathof,	TU Delft
	Ir. R. Van der Pluijm,	Raith BV

This thesis is confidential and cannot be made public until July 20, 2023.

TU Delft

Abstract

An ever-increasing demand for making microchips smaller and quicker pushes for the advancement of lithography machines. System dynamics plays an important role in determining the performance of a lithography machine. This thesis is aimed to increase the throughput of an electron beam lithography machine, mainly for sparse patterns, by improving the system dynamics. A detailed study was conducted to better understand the dynamics and possible limitations of the electron beam lithography machine. It was found that the stage motion generates a reaction force on the system, and this reaction force induces oscillations in the system resulting in the electron beam error. Furthermore, for sparse patterns, stage motion and electron beam settling consume most of the operation time. A solution method is proposed where an X-stage counter mass and a fourth-order trajectory generator is incorporated in the current system. This results in the elimination of system oscillations, reducing the settling time of the beam to zero and a reduction in stage motion time by 20%.

Acknowledgement

This project is a product of one year of extensive work carried out at Raith BV. I appreciate the opportunity to work on such an interesting topic.

I would like to express my special thanks to Ir. Ricardo Van der Pluijm for his constant support. I got to learn a lot from the weekly meetings with him. The insights he gave me about the machine and his feedback helped me steer the project in the right direction.

I would like to express my gratitude to Dr. Hassan HosseinNia for his guidance throughout the project. He provided valuable suggestions and also encouraged independent thinking and creativity.

I would like to thank Ir. Jo Spronck, I not only learnt from but also enjoyed the discussions with him during the Monday meetings.

I would also like to thank Ir. Koen Salden for his valuable feedback and assistance over the whole period of the project.

Lastly, I would like to thank my family and friends for their continuous encouragement and moral support.

Akash Kumar Jain
Delft, July 2021

Contents

Nomenclature

Symbols

c	Damping coefficient
f	Frequency
F	Force
k	Stiffness
m	Mass
Q	Quality factor
λ_e	Wavelength of the electron beam
ω	Angular frequency
ζ	Damping ratio

Abbreviations and Acronyms

AA 7075	Aluminium alloy 7075
AMC	Aluminium Matrix Composite
BLDC	Brushless DC motor
BSD	Backscatter electron detector
CAD	Computer-aided design
CoG	Center of gravity
CSR	Column support ring
e-beam	Electron beam
e.g.	exempli gratia, (for example)
EBL	Electron beam lithography
EBPG	Electron beam pattern generator
EOC	Electron optical column
et al.	et alia (and others)
i.e.	id est (that is)
IGP	Ion getter pump
FEA	Finite element analysis
FFT	Fast fourier transform
vs	versus

1

Introduction

The constant demand for the miniaturization of ICs and microchips has greatly motivated the semiconductor industry to make things smaller and faster. Raith BV has been working in the same direction with their electron beam lithography machine, the Electron Beam Pattern Generator (EBPG). To meet the high demand for superior (electron beam) lithography machines and prepare for the future, Raith continuously conducts research and development in-house and in collaboration with universities. This project is the result of one such collaboration with TU Delft, set up to study the dynamics of the EBPG for improvements.

This project looks into the system architecture of the EBPG, the effect of motion of the wafer stage on the system behavior, various methods to improve the system dynamics, and a detailed design of the proposed solution. For a better understanding of the project and the system, this chapter covers basic knowledge of electron beam lithography (EBL), the relevance of EBL in the field of micro-nano fabrication, components of EBPG and their functions, and an overview of the thesis.

1.1. Relevance

The everyday devices, from a smartphone to a car, use multiple microchips to function. This is evident from the disruption to the automobile industry caused by the recent global chip shortage [5]. These chips are manufactured with the help of lithography machines. Lithography is a process where desired patterns are etched on a material sheet called substrate by imparting energy-carrying particles. When the energy carriers are photons it's called photo-lithography and when the energy carriers are electrons it's called EBL. In photo-lithography, the whole surface or a part can be exposed at once. However, in EBL patterns are created by exposing one pixel at a time. This makes EBL a mask-less, but comparatively slow process. In photo-lithography the wavelength of light to be used is the limiting factor for resolution [3].Whereas for EBL, the wavelength of the electron beam (e-beam) can be varied. It depends on the energy of electrons [6]:

$$\lambda_e = \frac{1.226}{\sqrt{V}} \quad \text{(nm)}$$

Where V is the energy of the electrons in electron Volt (eV). Thus EBL can have a higher resolution compared to photo-lithography. The resolution of EBL is limited by the scattering of electrons in the resist [11]. Due to its higher throughput, photo-lithography dominates mass production, whereas EBL is mostly used for prototyping and research purposes. The capability to achieve higher resolutions also makes EBL apt for niche applications such as NEMS devices for health monitoring and space technology.

1.2. Electron beam lithography

EBL is a direct writing lithographic process, where a focused beam of electrons is used to form patterns by material modification, material deposition (additive), or material removal (subtractive) [12]. The steps of a generic EBL process are as follows: The substrate is first coated with a thin layer of electron-sensitive material called resist. The machine exposes the desired pattern with an e-beam pixel-by-pixel[1], which changes the local material properties of the exposed resist. After exposing one pixel, the e-beam moves to the next location on the substrate. This relative motion between the e-beam and the substrate is usually a combination of deflection in the e-beam, and motion of the substrate. The pattern exposure is followed by resist development and pattern transfer. Figure 1.1 shows a schematic of EBL.

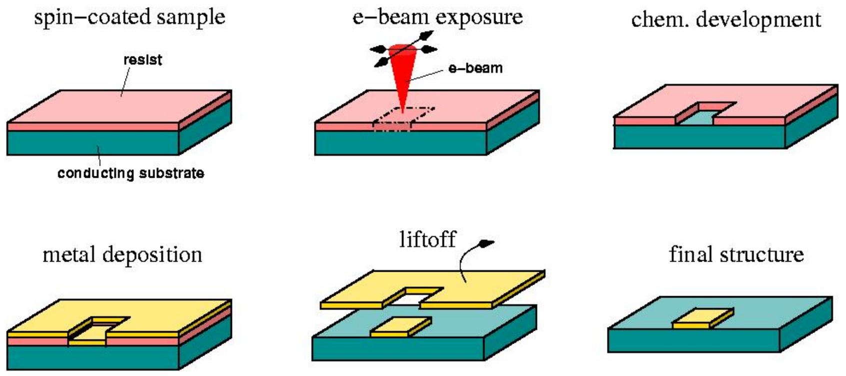

Figure 1.1: Steps involved in electron beam lithography[4]

1.3. EBPG5200

Raith manufactures EBL machines under the name Electron Beam Pattern Generator (EBPG), which has a Gaussian-shaped beam. There are two types of machines, EBPG5150 and EBPG5200, named after usable wafer sizes up to 150 mm and 200 mm respectively. This project is done keeping EBPG5200 in focus. From here onward, EBPG strictly means EBPG5200.

The EBPG can be divided into 3 main parts: electron optical column (EOC), exposure chamber, and a damped frame, as depicted in figure 1.2. The EOC generates, steers, and focuses the e-beam. The exposure chamber holds and positions the substrate. While the damped frame isolates the system from external vibrations.

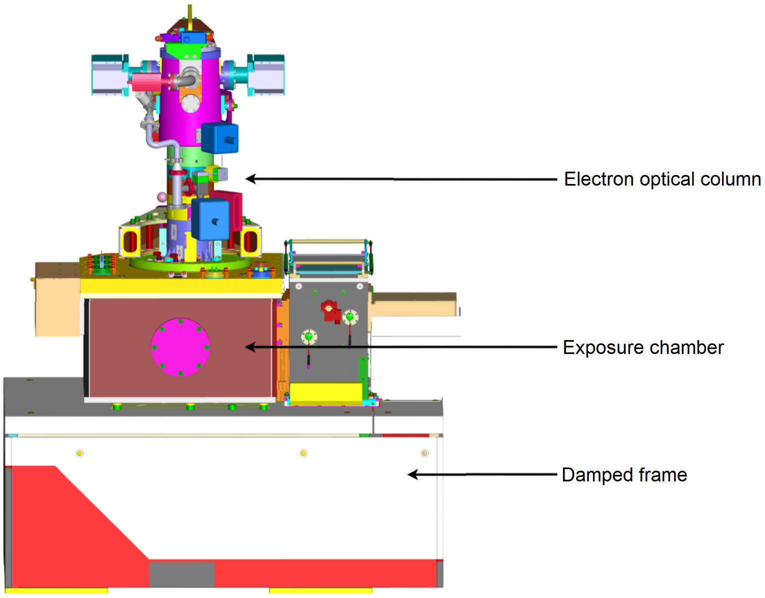

Figure 1.2: The EBPG5200 [18]

---

[1] A Gaussian beam shape EBL machine exposes the pattern in a pixel-by-pixel manner. However, a shaped beam system can expose certain shapes at once.

1.3.1. Electron optical column

The EOC consists of various parts to generate the e-beam, align it to the optical axis and finally deflect and focus it to the desired position. Figure 1.3 depicts the schematics of the EOC.

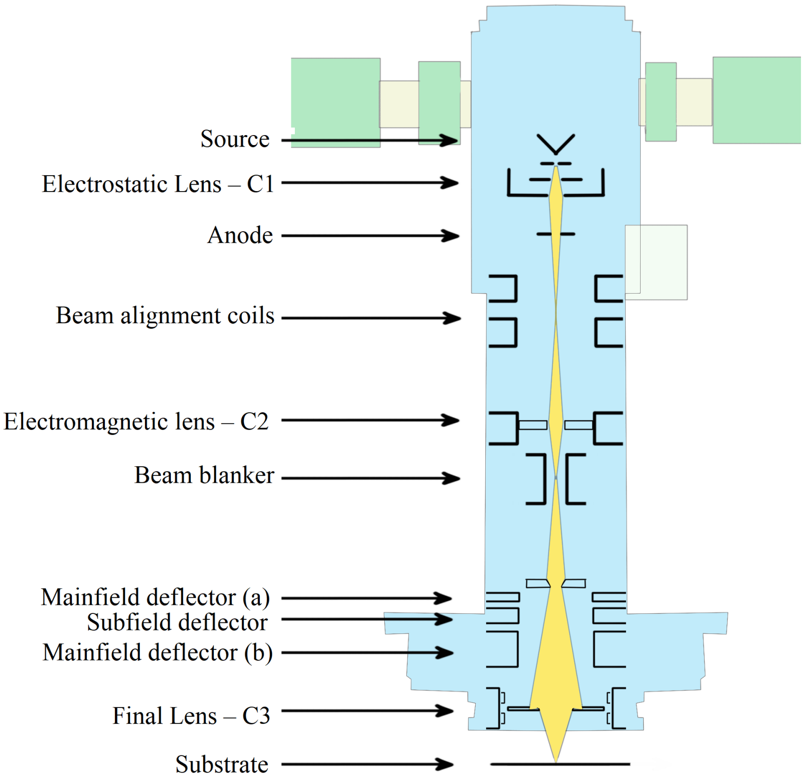

Figure 1.3: Schematic of the electron optical column

At the top of the EOC, a Schottky-type field emission gun is located which generates the e-beam. It contains a tungsten wire with a fine tip ($< 1\mu$m), that is heated to reduce its work-function [14]. And a high potential difference (up to 100 kV) is applied to remove and accelerate the electrons. The wavelength of the e-beam can be controlled by the applied potential difference. The e-beam then passes through an **electrostatic lens (C1)** which focuses the beam to the first cross over which lies near the beam alignment coils. The **beam alignment coils** can tilt and shift the beam to align it to the optical axis of the column. The co-axial beam then passes through an **electromagnetic lens (C2)** which focuses the beam to the second cross-over point lying in the beam blanker. Using the **beam blanker**, the beam can be deflected away from the optical axis, virtually disabling the beam. The beam then passes through a set of **deflectors** that corrects the gain, rotational error, keystone error and deflects the beam to the desired point. Lastly, the beam passes through the **final lens (C3)** which corrects for astigmatism and focuses the beam on the substrate.

Architecturally, the EOC is a vertical stack of hollow cylindrical steel structures with 2 ion-getter pumps (IGP) attached to it (*Appendix C.1: figure C.1*). It is mounted on top of the exposure chamber with the help of the column support ring (CSR). The CSR is a structurally strong ring made of Invar36®.

1.3.2. Exposure chamber

The exposure chamber is a cuboidal structure consists sidewalls and bottom plate made of steel, and top plate (also called vacuum cover) made of Invar36®. One of the side walls has a slit valve to load the substrate. This slit valve is connected to an airlock to maintain a vacuum inside the exposure chamber while loading a new substrate. A turbomolecular pump is attached to the bottom of the exposure chamber to create the vacuum. The substrate is mounted on a stage, this allows the displacement in the X and Y directions with respect to the electron beam. The XY stage hangs from the top plate with a stage suspension. This ensures a fixed distance between the EOC and the substrate and also makes the stage setup accessible for maintenance. A schematic diagram of the exposure chamber is shown in figure 1.4.

Figure 1.4: Schematic view of the exposure chamber

Stage suspension

The stage suspension is a closed box supported from the top. The top and bottom plates of the suspension are made of Invar36®, whereas side plates are made of aluminium alloy (AA 7075) . The walls of the stage suspension contain multiple venting holes for vacuum pumping.

Stage setup

The stage is mounted on the bottom plate of the stage suspension. The stage has three layers. The bottom layer is a **stationary plate**. On top of the stationary plate, the **Y plate** is mounted with the help of linear bearings, which allow the Y plate to move in ±Y direction. On top of the Y plate, the **X plate** is mounted with the help of another set of linear bearings allowing motion in ±X direction. These motions in X and Y directions are provided by two separate BLDC motors and rack-and-pinion mechanisms. The X plate holds a substrate support block called **superplate**, which allows the mounting of a substrate holder and has two perpendicular inbuilt mirrors for Interferometry (see *Sensors*). Due to the stacked setup, the Y plate also carries the X plate with it.

The stationary plate is mounted on top of two blocks which are replaceable with piezo-actuators to provide optional Z motion. Figure 1.5 shows various parts of stage setup.

Figure 1.5: Stage setup

1.3.3. Damped frame

The exposure chamber along with the electron optical column is mounted on a damped frame. The damped frame contains four air dampers on four corners, controlled by three valves. The air dampers isolate the system from external disturbances.

1.3.4. Sensors

Being a high-tech system, the EBPG is equipped with several sensors. The two main types of sensors are as follows:

Interferometers

The stage motion is controlled by a closed-loop controller requiring a sensor. To measure the position and the velocity of the XY stage and provide feedback to the controller, 2 heterodyne double pass interferometers are mounted to the top plate of the suspension assembly.

A heterodyne interferometer works on the principles of **interference of light** and **doppler effect**. It uses a laser light comprised of 2 distinct frequencies, hence the name heterodyne. The light passes twice between the interferometer and the superplate, this doubles the resolution. Additionally, digital interpolation is done to improve the resolution further. The interferometers used in the EBPG have a resolution of 0.155 nm.

Backscatter electron detectors

To precisely locate datum[2] targets on the substrate and calculate necessary beam corrections, backscatter electron detectors (BSD) are provided. These also allow for imaging like an electron microscope.

The BSDs collect the backscattered electrons and using a photomultiplier and convert them to a proportional electric current. The substrate holder contains a square marker at a known position (datum target), usually at the corner. The marker has high electron reflectivity. Hence, the number of backscattered electrons varies when the beam moves in or out of the marker and this can be used to determine the marker edges, as shown in figure 1.6. By scanning the beam through the marker twice, parallel to the two adjacent edges, the center of the marker can be located with ~nm accuracy.

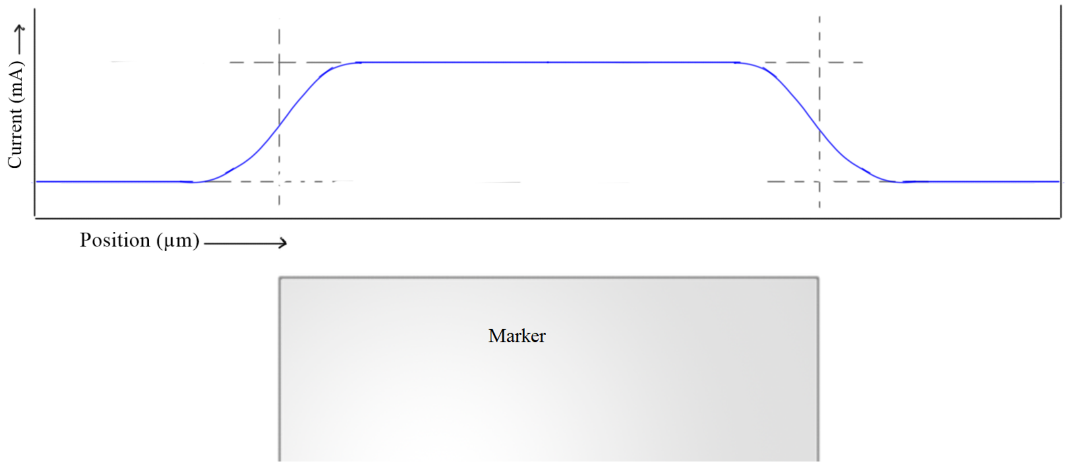

Figure 1.6: Current v/s position plot of BSD data showing **edge detection**

By recording the electric current values from the BSDs while scanning the beam perpendicularly over the marker edge, we can get the **current v/s position** plot (or sensitivity). By focusing the e-beam on one of the edges and using the sensitivity, an **error v/s time** plot can be generated. This method is called **Beam-on-Edge**.

1.3.5. Stage controller

The XY stage is moved using 2 BLDC motors and rack-and-pinion mechanisms. Each BLDC motor is controlled by two **PI controllers** in series. The first controller is responsible to match position setpoints

---

[2] Datum: a fixed starting point of a scale or an operation.

and the second controller is responsible to match velocity setpoints. The controller receives the position, velocity, and acceleration setpoints from a **sinusoidal trajectory generator**, and position and velocity feedback from the interferometers.

The generated acceleration is a function of sine, hence the name sinusoidal trajectory. The acceleration is integrated once to find the velocity trajectory and integrated twice to find the position trajectory. The generated trajectory has maximum limits for acceleration and velocity. Therefore, for longer steps, the trajectory has a constant velocity phase. Figure 1.7 shows plots for acceleration, velocity, and position as functions of time for a typical sinusoidal trajectory.

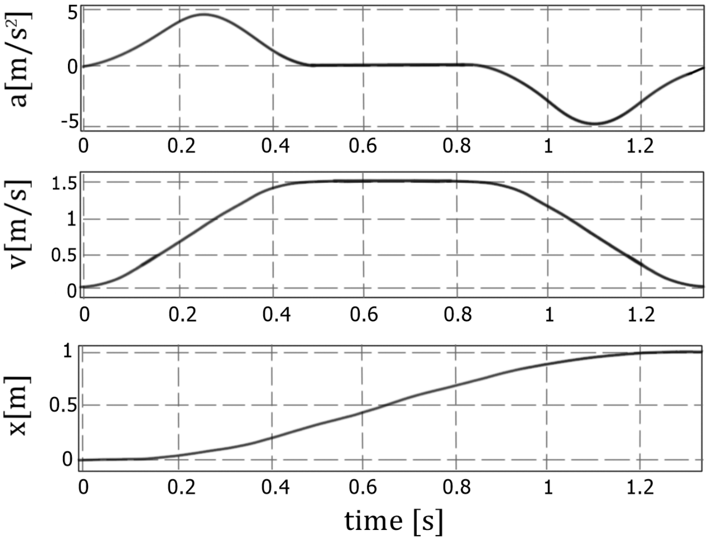

Figure 1.7: Sinusoidal trajectory: Acceleration, velocity and position plots

These trajectories are then converted to respective setpoints. On top of the PI controllers, some feedforward control and filters are used too. The control has two noise sources (Noise Scr 1 & 2), in case an intentional noise has to be introduced in the control loop. A block diagram of the controller is shown in figure 1.8.

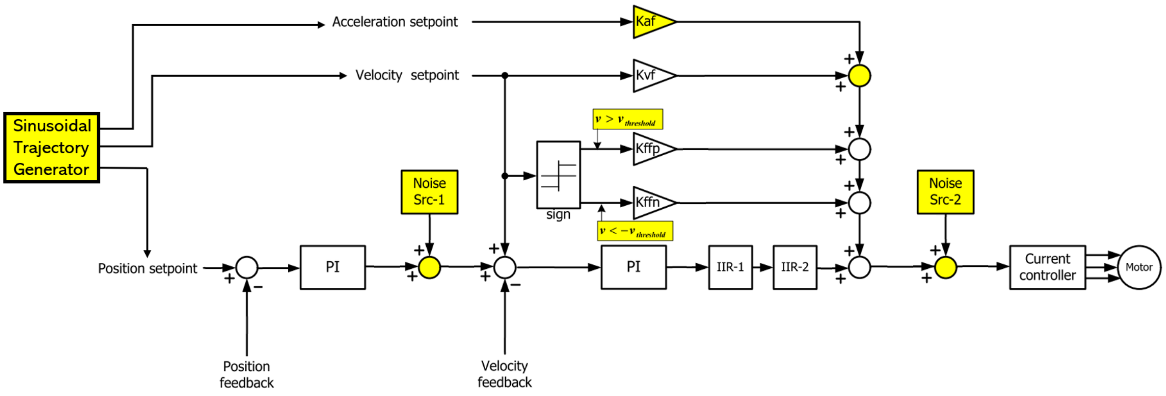

Figure 1.8: Stage controller

1.3.6. Writing Strategy

As stated before, the EBPG exposes the desired pattern one pixel at a time. To expose the whole pattern, there should be a relative motion between the e-beam and the substrate. Both the beam and the substrate are capable to move independently. The e-beam has a motion restricted to ±0.5 mm around the optical axis. That means the write field is 1 mm x 1 mm. Hence the substrate is virtually divided into a grid of square blocks of area 1 mm^2 each. These blocks are known as main write fields or **main fields**.

The writing is done in several steps: the stage (along with the substrate) is moved such that the e-beam coincides with the center of a main field. Once the substrate is within a certain range from the desired position, the interferometer signal can be used to correct the beam and compensate for the position error in real-time. From this point on, the writing can be started. This range is called **window** and it is set to $\pm 1.25\ \mu$m. The electron beam can move and expose a whole main field. After which the stage moves the substrate to the next main field. And the process repeats until the whole pattern is exposed.

Furthermore, the stage motion generates vibrations in the system which in-turn cause error in the e-beam. To avoid any errors in the pattern due to the beam vibrations, an additional settling time is given before starting the exposure. The recommended settling time is 100 ms. Figure 1.9 shows a typical stage move.

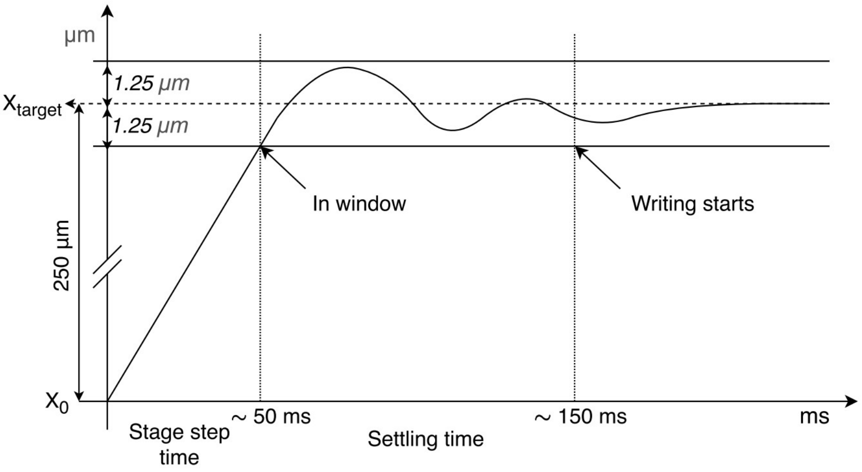

Figure 1.9: Position v/s time plot for a typical stage move [18]

To summarize, the writing process follows move (the substrate), settle (the e-beam), expose, and repeat.

1.4. Thesis aim and scope

The EBPG ticks all the right boxes in the quality column but performs poorly in terms of speed and throughput. The thesis aims to increase the throughput without compromising the quality by improving the system dynamics.

The thesis is mainly focused to increase the throughput for **sparse patterns**[3]. Sparse pattern writing is one of the important aspects of the EBPG. For sparse patterns, the stage motion and the e-beam settling can take up to 99% of the total writing time. Reducing these time components can greatly increase the system throughput. Hence this thesis looks into various methods to reduce the stage motion and the beam settling time.

The thesis progresses as follows: in chapter-2, a detailed system evaluation is conducted that includes a qualitative design evaluation and a quantitative experimental analysis. Chapter-3 discusses a set of requirements for the desired solution method. In chapter-4 a simplified model of the system is developed. Chapter-5 contains numerous concept designs fulfilling the discussed requirements and a detailed shortlisting process to choose a final solution method. In chapter-6, the selected solution method is developed in detail and validated. At last, chapter-7 provides the conclusion of the project and other recommendations for further improvements.

---

[3] Sparse pattern: when the pattern is distributed such that there is relatively less writing per unit area.

2

System evaluation

A wide range of design and experimental analyses are conducted to better understand the system behavior and identify possible limitations of the current system. In section 2.1, the design evaluation of the system is discussed. It elaborates the metrology loop, force loop, and thermal loop, along with their relation to system architecture. Section 2.2 contains theoretical process analysis to compare the timeshare of different exposure steps for various pattern types and numerical comparison between the number of X-steps and Y-steps. Section 2.3 discusses experimental analyses and their results. It includes studies of stage motion, system vibrations, and their effect on the e-beam.

2.1. Design evaluation

2.1.1. Metrology loop

A metrology loop is defined as a closed-loop starting from the measurement device passing through the support structure to the point of interest, such that dimensional changes to any member parts would not be detected by the measurement process [17]. For EBPG, there are two types of sensors therefore two separate metrology loops.

For the interferometer, the metrology loop starts from the interferometer passing through the mounting, top plate of stage suspension, vacuum cover, CSR, and e-beam to the substrate. The metrology loop for the interferometer is depicted in figure 2.1. Any deformation in the metrology loop can cause an error in the measurement, this also results in deviation in e-beam position on the substrate. The deviation in e-beam position has to be emphasized as **the desired measurement is the position of the substrate with respect to the e-beam, however, the measurement here is the position of the superplate mirror with respect to the interferometer.**

Figure 2.1: Metrology loop for the interferometer

The metrology loop for the BSD is a line passing through the e-beam, starting from the EOC and ending on the substrate. This metrology loop is a line because both the end effector and the measuring element are the same, the e-beam.

2.1.2. Force loop and stiffness

For static equilibrium, the sum of all forces on a system has to be zero. Hence, for any force applied to a sub-system, there will be a loop of structural elements around which this force is transmitted. This is called the force loop [17]. The force loop runs from the end-effector through supporting structure to point of interest on the workpiece. In EBPG, the force loop runs from the bottom of EOC through CSR, vacuum cover, stage suspension, and stage assembly to the substrate as shown in figure 2.2. The structural elements in the force loop get deformed due to this force. If the force loop coincides with the metrology loop it will cause an error in the measurement. To avoid the deformation, **the forces and moments in the force loop can be reduced and the structure can be made stiffer**.

Figure 2.2: Force loop

It is to be noted that the force loop can also affect other structural elements rigidly connected to the elements in the loop.

Problem(s): It is observed that the metrology loop for the interferometer and the force loop coincide over the suspension top plate, vacuum cover, CSR, and the EOC. Also, the interferometer is directly mounted to the suspension top plate, and forces on the suspension top plate can cause vibrations in the mounting. This can result in measurement errors.

The metrology loop for the BSD coincides with the force loop over the EOC. This can cause errors in the e-beam position.

Mitigation: To make the stage suspension stiff, it is designed to be a closed cuboid. Additionally, the side plates are slanted inwards going down for increased stiffness. The vacuum cover and the CSR are designed to have a low aspect ratio for high stiffness. On top of that, the actuation force is also kept low by limiting the maximum acceleration of the stage.

These methods help reduce the vibrations but do not fully solve the problem. For instance, the EOC is only supported from down (by the CSR) which results in low stiffness of the EOC with respect to the exposure chamber. As a result of this, the stage motion causes vibrations in the EOC, hence an additional time has to be provided to settle down the vibrations (as stated in section 1.3.6).

2.1.3. Thermal loop and material selection

Components in a mechanical assembly are subjected to heat loads due to thermal expansion with varying temperatures. A thermal loop is defined as a close loop passing through mechanical components which determine the relative position of specified objects under changing temperatures [17]. For the EBPG, the specified object is the substrate and its position has to be measured relative to the e-beam. The thermal loop for the system is shown in figure 2.3.

Problem: Any **horizontal** deformation in the thermal loop would cause a position error in the e-beam and measurement error for the interferometer.

Mitigation: The main mode of the heat transfer into the system is due to convection from the environment. However, within the system heat is mainly transferred due to conduction from surface elements[1]. To decrease the heat conduction into the exposure chamber, thermal coupling between the vacuum cover and the suspension top is reduced by providing a 2mm gap from few centimeters from the column opening to the edge of the suspension top plate. Additionally, the vacuum cover is liquid-cooled along with other heat sources inside the system, such as the BLDC motors.

To avoid the horizontal deformation in the thermal loop a few methods are implemented. To avoid any dimensional changes to the substrate, the superplate is made of Zerodur, a glass-ceramic with an extremely low coefficient of thermal expansion of $0.02 \times 10^{-6} K^{-1}$. And the superplate is mounted using a maxwell kinematic coupling to the X-stage. For the CSR, the vacuum cover, and the top-bottom plates of the suspension, Invar is used, which also has a low thermal expansion coefficient ($1.2 \times 10^{-6} K^{-1}$). For stage assembly, X and Y plates are made of the same material, aluminium matrix composite (AMC®). The stationary plate is made of AISI316 which have nearly the same thermal expansion coefficient as AMC (*Appendix A*). The close values of the thermal expansion coefficient ensure the similar thermal expansion of all three plates. And due to isotropic expansion[2], there will be no bending, just planar expansion. For the planar expansion is of the stage plates is the thermal center coincide with the geometric center. The maxwell coupling of the superplate is designed around the thermal center of the the X-plate. Therefore the superplate remains isolated from the stage expansion.

The interferometer mounting is also made of Invar to make the metrology loop thermally stable.

Figure 2.3: Thermal loop for the e-beam and chosen materials

2.1.4. Vacuum

The electrons need a vacuum to travel efficiently, otherwise, they will collide with air molecules and lose energy. Hence, a high vacuum is maintained from the EOC to the exposure chamber. To create a vacuum a turbomolecular pump is attached to the bottom of the exposure chamber. The exposure chamber has a pressure of 10^{-7}mbar. The EOC needs an even higher vacuum (10^{-9}mbar), for this purpose two ion-getter pumps are mounted to the EOC.

2.1.5. Magnetism

The e-beam is highly sensitive to magnetic fields. Moving electrons inside a magnetic field experience Lorentz force and can divert from their path. To isolate the e-beam from environmental fields steel shrouds and MuMetal shields are used. The main sources of undesired magnetic fields inside the system are BLDC motors. Therefore, MuMetal is used to shield the magnetic fields of the BLDC motors.

---

[1] System elements exposed to the environment/air

[2] Isotropic expansion because of high thermal permeability of AMC.

2.2. Theoretical process analysis

2.2.1. Pattern types and the main time-consuming step

A study is conducted by Raith regarding the time taken by various exposure steps for different types of patterns[8]. As seen in figure 2.4, for dense patterns the e-beam is active for most of the time. However, for the sparse patterns (Gate) stage settling (stage motion + beam settling) consumes a big portion of the time and for complex patterns, pattern calculation consumes most of the total time.

Figure 2.4: Pattern types and time share for various exposure steps[8]

This thesis is aimed to increase the throughput in the case of sparse patterns. Hence the focus is kept on reducing the stage move time and settling time.

2.2.2. Stage motion: X-step vs Y-step

As discussed in section 1.3.2, there are two types of stage motion: in the X direction and Y direction. The X stage can move independently unlike the Y stage which has to carry the X stage with it. Hence, the X step is preferred over the Y step. A comparison is done for a pattern where every main field has to be exposed as shown in figure 2.5.

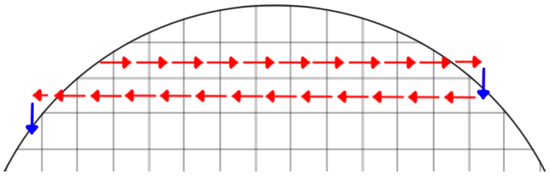

Figure 2.5: Typical stage motion, where Red arrows represent motion in X direction and blue arrow represents motion in Y direction

The X steps are used to move along a row. The total number of X steps will be the number of main fields on the substrate minus the number of rows. And Y steps are taken only after exposing all main fields in a row to move to the next row, the total number of Y steps will be the number of rows of main fields on the substrate minus one. The following calculation shows a comparison between the number of X steps and Y step,

Number of steps in X direction = $\pi \times R^2 - 2R$
Number of steps in Y direction = $2R - 1$, where is R is the radius of a wafer in mm, i.e. 100 mm
Ration of number of X steps and Y step = $\frac{\pi\times R^2-2R}{2R-1} = \frac{10000\pi-200}{200-1} \approx 157$

It can be presumed that decreasing stage move time and settling time for X step alone can improve the throughput substantially.

2.3. Experimental analyses

2.3.1. Stage motion and control

An experimental study is conducted on the stage motion. The stage is moved a particular distance in X or Y direction while the velocity and position data are recorded using the interferometers and motor current is recorded from the controller. The acceleration is calculated by differentiating velocity data. In total 16 sets of measurements were recorded for step sizes: 0.045 mm, 0.25 mm, 1 mm, and 80 mm in all four directions i.e. ±X and ±Y.

As discussed in section 1.3.5, the stage has a sinusoidal trajectory. The generated trajectory has maximum limits for acceleration and velocity. The maximum acceleration for X stage is 0.9 m/s^2 and for y stage it is 0.4 m/s^2. The velocity limit is 40 mm/s in both directions. The data from the experiment is used to find the time taken for various step sizes and validate the velocity, and acceleration limits. And the acceleration data is differentiated once to find maximum jerk and twice to find maximum snap (the fourth derivative of position)(*see Appendix B.1.2*).

A second experiment is conducted to find the frequency response of the stage. A random noise signal is injected into the stage via the motor controller (using Noise Src-2 as shown in figure 1.8). Using the interferometer, the system (position) response is recorded. The motor current (I_q) is used to calculate the force (F) on the stage.

$$F = I_q \times K_m / r_p$$

where, K_m is the motor constant and r_p is the radius of the pinion.

From the recorded data following two transfer functions are estimated (using *tfestimate* function and *Hann window* in MATLAB).

$\mathrm{TF}_{\mathrm{output}}$ = transfer function between stage position and injected noise
$\mathrm{TF}_{\mathrm{input}}$ = transfer function between force and injected noise

Using the two transfer function, the close-loop frequency response for the stage is found. Where,

$$\mathrm{FRF}_{\mathrm{plant}} = \mathrm{TF}_{\mathrm{output}} / \mathrm{TF}_{\mathrm{input}}$$

The bode plot of the frequency response function (FRF) of X-stage is obtained by the close loop analysis. The plot is shown in figure 2.6.

Figure 2.6: Bode plot for the transfer function between the X stage position and force

It is observed that the bandwidth for X-stage is 25 Hz and for Y-stage is 28 Hz (*Appendix B.2*).

2.3.2. Vibrations and frequencies

To understand the dynamic behavior of the system a set of experiments are performed using 3 accelerometers mounted on the EOC, the vacuum cover, and the damped frame as shown in figure 2.7. These experiments provide information on force transmission, vibration amplitudes, and excitation frequencies. The accelerometers measure the acceleration amplitude along its axis. Using accelerometer data, the acceleration v/s time graph can be plotted. By performing fast Fourier transformation (FFT) on the time domain data, frequency components of vibrations can be obtained.

Figure 2.7: Schematic diagram of the EBPG showing locations of accelerometers (red, green and blue blocks)

The first part of the experiment is conducted in two sets, keeping the damped frame disabled and later enabling the damped frame. In both cases the stage is kept stationary. This experiment is conducted to understand the effect of the damped frame on the system dynamics and measure the background frequencies[3].The experiment shows that **the damped frame is also capable to damp the lower frequency (up to 200 Hz) internal vibrations** (depicted in figure 2.8). The data from the experiment also shows that the system has vibrations with background frequencies 333 Hz, 444 Hz, and 459 Hz when the damped frame is enabled. The frequencies 444 Hz and 459 Hz are due to the turbomolecular pumps attached to the system. 333 Hz is dominant on the damping table, this might be an eigenfrequency of some part of the frame or sheet metal cover.

Figure 2.8: Frequencies comparison for damped frame enabled (Red plot) and disabled (Blue plot). The lower frequency are not dominant in ground vibrations (*Appendix B.4*)

---

[3] Background frequencies: frequencies present in the system without external excitation, in this case, the stage motion.

The second part of the experiment is done while keeping **the damped frame enabled and moving the stage** with a small step either in X or Y direction at a timeFigure 2.9 shows the acceleration v/s time plot for 3 accelerometers when the stage is moved 1 mm in the X-direction. The plot is divided into 3 parts. Part **I**, before stage motion, mainly consist of 444 Hz and 459 Hz. Part **II** contains stage motion and settling, and part **III**, after the payload-induced vibrations[4] are settled.

Figure 2.9: X- direction acceleration v/s time plots for stage motion of 1 mm in X-direction. Where, **Top**: top of the EOC, **VC**: on the vacuum cover, **Table**: top of the damped frame

By performing FFT on the acceleration data, various frequency components of vibrations are observed as shown in figure 2.10. Other than the background frequencies (333 Hz, 444 Hz, and 459 Hz), a frequency band from 5 Hz to 35 Hz is observed on all three accelerometers. The accelerometer on the optical column also observes frequencies around 163 Hz.

Figure 2.10: Frequencies present at various positions

---

[4] Vibrations caused by stage motion

To further study the effect of the stage motion on system dynamics, two bandstop filters are applied at 444 Hz and 459 Hz on the accelerometer data. The filtered data is plotted in figure 2.11.

Figure 2.11: X- direction acceleration v/s time plots of data with bandstop filter at 444 Hz and 459 Hz for stage motion of 1 mm in X-direction

In figure 2.11, the acceleration plot for the vacuum cover shows that the stage motion creates a sinusoidal reaction force on the vacuum chamber. The accelerations in the plot are absolute accelerations. They also contain acceleration of rigid body mode of the full system and that doesn't affect the system performance. The frequency of the sine function of the reaction force should depend on step size. For smaller steps (with no constant velocity phase) the frequency of excitation will be reciprocal of the time required for the step.

For X-step of 1 mm, the step time is 0.084 s (*Appendix B.1.1*). Hence the excitation frequency will be $f = 1/0.084 \approx 12Hz$.

Also, it is observed that **the exposure chamber has nearly half the acceleration amplitude compared to the EOC and after the sinusoidal excitation the exposure chamber settles quickly. Whereas, the EOC takes more than 100 ms longer to settle**.

The effect of the X-step in the Y-direction and the effect of the Y-step in the X-direction is studied as well (*Appendix B.5*). It has been observed that for small steps the X-step doesn't create vibrations in Y-direction and vice versa.

However for longer steps (50 mm here), the stage motion in the X-direction cause vibrations on the damped frame in Y-direction. And the step in Y-direction creates vibrations in both directions X and Y at all three positions. However, there are no residual vibrations in the X-direction after the stage finishes the step in Y-direction.

2.3.3. Beam-on-Edge

To observe the effect of the stage motion on the beam, an experiment is conducted where Beam-on-Edge is used to measure the beam error. The experiment method is as follows: the stage is moved a small step to the marker edge; once the stage is in window, the Beam-on-Edge measurement is started. Figure 2.12 shows beam error v/s time plot for stage motion of 250 μm in X direction.

And FFT of this data shows the frequency components of the beam error. Figure 2.13 shows a comparison between frequencies present before and after the stage motion. The vibrations of the e-beam contain 50 Hz and its multiples, 60 Hz, a frequency band around 250 Hz, 444 Hz, and 459 Hz. The 50 Hz and its multiples are because of AC frequency, 444 Hz and 459 Hz are due to the turbomolecular pumps. 60 Hz and the 250 Hz frequency bands are because of the stage motion. It is

Figure 2.12: Beam error v/s time plot after step of 250 μm in X direction

Figure 2.13: Frequency components of the beam error after stage motion of 250 μ m in X direction. The red plot shows background frequencies and blue plot shows effect of stage motion on the beam

also observed that the 60 Hz and 250 Hz bands are independent of step size.

Recalling the metrology loop of the BSD, the error in the e-beam can be caused by the EOC vibration and/or the stage vibration. And when the stage is in window, the interferometer signal is used to correct the beam. Therefore, the interferometer vibration can also cause error in the e-beam. Any non-synchronized vibration of the stage or the interferometer can be measured from the interferometer.

Comparing the interferometer data (*Appendix B.1.3*) and the accelerometer data with the e-beam error it has been observed that the EOC and the e-beam oscillate for nearly the same time. Whereas the stage settles within half of the time with respect to the interferometer for the same step size. It can be inferred that the main contributer to the e-beam error is the EOC vibrarion.

The measurement method for the e-beam is limited by shot noise[5], beam jitter, electromagnetic interference etc. Therefore, the e-beam will always have some intrinsic noise. Even without the stage motion, **the e-beam has an error of ±2 nm**. This ±2 nm error is the result of all error sources (AC current, turbomolecular pumps and shot noise, etc).

The experiment is also conducted with stage motion in the Y direction (see *Appendix B.4*). It is observed that payload induced vibrations for Y-direction comprise of frequencies 32 Hz, 64 Hz, and 80 Hz, also independent of step size.

---

[5] Shot noise limited due to the particle nature of the electrons

2.4. Summary

- The interferometers measure superplate mirror position, not the e-beam position on the substrate. This makes the system vulnerable to error due to vibrations in the EOC.
- The force loop partially coincides with the metrology loop, this can cause measurement error due to deformation in the force loop.
- Any thermal changes can cause an error in the e-beam and the interferometer measurements. However, with a smart selection of materials, reducing thermal coupling, and using actively controlled coolant the effect is reduced.
- The system needs to maintain a high vacuum and is sensitive to magnetic fields.
- The stage motion and settling consume most of the time for sparse patterns.
- The X stage moves more than 150 times compared to the Y stage for a uniform sparse pattern.
- The X stage has 25 Hz bandwidth and the Y stage has 28 Hz bandwidth.
- The damped frame also damps the lower frequency internal vibrations.
- The EBPG has background vibrations of frequencies 333 Hz, 444 Hz, and 459 Hz.
- The payload-induced vibrations for the system[6] are function of step size.
- The EOC has a higher amplitude of payload-induced excitation compared to the exposure chamber. And the EOC takes longer to settle.
- For smaller steps, the stage motion in the X-direction doesn't create vibrations in the Y-direction and vice versa.
- For long steps, The stage motion in one direction can create vibrations in the other direction but they damp as the stage finishes the step.
- The EOC vibrations cause an error in the e-beam position.
- The payload-induced vibration's frequency for the e-beam are independent of step size. However amplitude is directly proportional.
- The e-beam has noise of ±2 nm, without the stage motion.

---

[6] Dynamic vibrations, not the e-beam error

3

Design requirements and environmental conditions

The solution method has to fulfill certain requirements and function within given constraints. This chapter discusses the key requirements for the solution method, environmental conditions under which the solution has to perform, mechanical constraints, and other additional requirements.

3.1. Solution requirements

This project aims to increase the throughput without compromising the quality, mainly for sparse patterns. As discussed in section 2.2.1, for sparse patterns stage motion and settling are the most time-consuming operations. And stage motion in X-direction is more frequent than Y-direction. Hence the primary objective is to minimize the X-direction stage motion and the beam settling time.

To quantify the requirements two types of stage motion (in X-direction) are selected based on the step size, small steps, and large steps. There is no constant velocity phase for smaller steps (step size < 3mm) during the stage motion. Being the most frequent step size, 1 mm steps are considered for this category. And for large steps, an 80 mm step size is chosen. The current values and target values for various parameters are listed in the table 3.1.

Table 3.1: Solution requirements

Parameter	Current value	Target value
	Step size : 1mm	
Stage motion time	83.6 ms	<70 ms
Beam settling time	100 ms[1]	<50 ms
	Step size : 80mm	
Stage motion time	2.07 s	<1.70 s
Beam settling time	100 ms[1]	<50ms

The stage motion time is defined as the time taken to move the stage within the window for given step size. The beam settling time is defined as the time required to settle the e-beam such that the error from the desired position is within **±2 nm**.

The stage motion time and beam settling time can have a reciprocal relationship, as increasing the stage acceleration to reduce motion time will cause higher amplitude vibrations on the e-beam. Thus increase the e-beam setting time. This is one of the reasons for the acceleration limit of stage motion.

A new parameter, **stage settling time**, is defined here. The stage settling time is the sum of the stage motion time and the e-beam settling time. Stage settling time for **1mm step is 183.6 ms and for**

---

[1] A fixed setting time is defined for all step sizes.

80mm step is 2.17 s.

3.2. Environmental conditions

The EBPG is operated in a cleanroom environment and any solution method also has to be capable to function under the same environmental conditions. These environmental conditions are listed in table 3.2.

Table 3.2: Environmental conditions[1]

Parameter	Value	Remarks
Temperature (operational)	292-294K	20±1°C
Temperature (during transport)	288-298K	20±5°C
Temperature gradient inside chamber	≤0.1K/h	
Pressure cleanroom	10^5 Pa	1 bar
Pressure inside chamber	10^{-5} Pa	10^{-7} mbar
Relative humidity	40-70%	
Acoustic noise	≤65dBA	
Magnetic field deviation	$\leq 4\times10^{-8}$T/h	
Magnetic stray-field	$\leq 5\times10^{-8}$T	Peak-peak for both vertical and horizontal plane
Ground stiffness	$\geq 53\times10^{6}$N/m	
Ground vibrations	<10μm/s	For all frequencies

All design changes in the system have to be compatible with a given temperature range. However, thermal stress and expansion are allowed during transport up to a limit unless they permanently deform any part of the system.

All design changes inside the exposure chamber have to be vacuum compatible. This means materials with a high outgassing rate are not allowed. And any shapes with trapped air pockets, known as virtual leak, have to be avoided as well.

3.3. Mechanical constraints

The mechanical constraints mostly affect any modification inside the exposure chamber. These constraints are listed in table 3.3.

Table 3.3: Mechanical constraints

Parameter	Value	Remarks
Volume exposure chamber	696x760x385 mm^3	
Volume suspension asembly	540x607x293 mm^3	
Optical working distance	40 mm ±50 μm	Height between stage and final lens (Hard constraint)
Space underneath stage	≤70 mm	Space needed for optional Z-stage (Soft constraint)

Any modification to the stage has to fit inside the suspension assembly. The distance between the substrate and the final lens has to remain constant, i.e. the fidelity of substrate placement with respect to the EOC is a hard constraint. The space underneath the stage is a soft constraint. A smaller Z-stage can be used to reduce this space.

3.4. Additional requirements

3.4.1. Magnetism

The e-beam is highly susceptible to the magnetic field. Therefore, any unavoidable magnetic parts such as actuators have to be kept away from the EOC and the substrate. Also, the magnetic subsystems can be shielded using MuMetal.

3.4.2. Material properties

The material selection for any modification has to be done considering the following requirements:

- The materials used inside the exposure chamber should be vacuum compatible.
- Any materials used nearby the e-beam should be either a conductor of electricity or coated with a conductive layer to avoid charging[2].
- Materials used near the EOC should have high magnetic permeability to avoid any inference with magnetic fields of the EOC.

3.4.3. Maintainability

The EBPG is equipped with a crane to disassemble the exposure chamber for maintenance. Any modification to the system should be done keeping in mind easy access to the exposure chamber.

---

[2] Charge buildup due to accumulation of scattered electrons

4

System modeling and simulation

It is not practical to test each solution method on the real system. For this purpose, a simplified model is developed. The model is developed using first principle equations. The system parameters are tuned using finite element analysis (FEA) and validated with the experimental data. This chapter discusses system modeling and validation.

4.1. Lumped mass-spring-damper model

The EBPG is divided into 4 lumped masses as listed in table 4.1. The masses of system parts are calculated using the CAD models. The mass value of 4 lumped masses is calculated by adding the mass of member elements (*Appendix C.1*).

Table 4.1: Lumped masses and their member elements

	Member elements	**Mass**
m_1	Damped frame, turbo pump, crane, bottom plate of exposure chamber	904 kg
m_2	Exposure chamber (top plate, side plates), CSR, top plate of suspension	562 kg
m_3	Stage assembly, suspension (except top plate)	111 kg
m_4	EOC (Shrouds, outer bucket, inner bucket, ion getter pumps, etc)	120 kg
	Total mass	**1695 kg**

During the X-stage motion, it imparts a reaction force on the system. Hence in the model, the mass m_3 doesn't contain the mass of the X-stage and an actuator is placed between m_3 and x-stage. The mass of x-stage (m_x) is 11.6 kg.

As observed in section 2.3.2 (figure **??**), the stage motion in one direction doesn't have residual vibrations in another direction. To model the system behavior it is assumed that the motion of system parts is linear, horizontal, uni-dimensional, and independent of motion in other directions. Therefore, two separate lumped mass-spring-damper models are designed to study X and Y motion independently. The model for X and Y direction have nearly the same parameters other than the mass m_3 and stage mass. The mass m_3 for the Y-direction model will be 101 kg and stage mass m_y will be 21.6 kg, because the Y-stage moves X-stage with it.

In the model, the masses are connected to each other with linear springs and dampers as shown in figure 4.1. The stiffness (k_1) and damping coefficient (c_1) for the damped frame are calculated using the transmissibility plot of the air dampers. Stiffness for exposure chamber (k_2), stage suspension (k_3) and the EOC (k_4) are calculated using FEA (*Appendix C.2*). The standard damping ratio of a metal structure with joints is used to calculate the damping coefficients of the exposure chamber (c_2) and the stage suspension (c_3). And for the EOC (c_4) the standard damping ratio of large diameter pipe is used[13] (*Appendix C.3*). The stiffness and damping coefficients are listed in table 4.2.

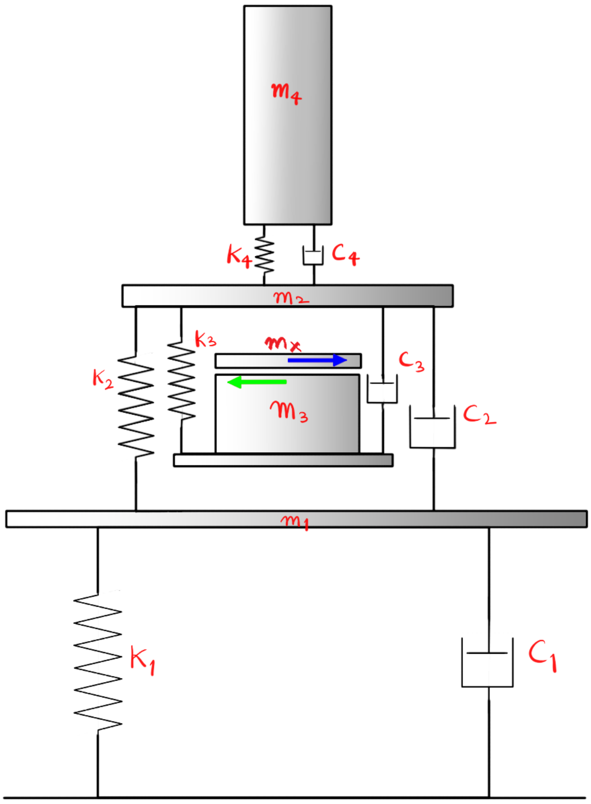

Figure 4.1: Lumped mass-spring-damper model of EBPG. The blue arrow represents stage motion and green arrow represents reaction force on the system

Table 4.2: Model parameters: Stiffness and damping coefficient

	Stiffness (N/m)		Damping coefficient (Ns/m)
k_1	2.6×10^5	**c_1**	3.5×10^3
k_2	2.5×10^9	**c_2**	2.0×10^5
k_3	5.0×10^8	**c_3**	3.4×10^4
k_4	5.3×10^6	**c_4**	1.2×10^3

4.2. Simulink model and validation

The lumped mass-spring-damper model is replicated in MATLAB Simscape for simulations. The Simscape model is shown in figure 4.2.

To actuate the stage a custom sinusoidal trajectory generator is created. The trajectory generator in the model calculates acceleration for the given step size and converts it to force by multiplying it with stage mass m_x. The trajectory generator applies the force on the stage via an actuator block. The actuator block is mounted on the mass m_3 and applies a reaction force on m_3.

Various sensors are used on the system to study the model behavior. Three force sensors are used to measure the forces on three masses, m_1, m_2, and m_4. Later these forces are converted to accelerations by dividing the force by the respective masses. Three motion sensors are used to measure positions of the stage, mass m_2, and mass m_4. And the EOC (m_4) position is plotted with respect to the exposure chamber (m_2).

To validate the model, the simulation results are compared with the experimental data. The acceleration vs time plots for the EOC (m_4), the exposure chamber (m_2), and the damped frame (m_1) are compared with the plots of experimental data (figure 2.11). The acceleration plots from the simulation are shown in figure 4.3.

It is observed that the simulation results have similar behavior as the experimental data. For instance, all three masses experience the sinusoidal accelerations due to the reaction force, the EOC

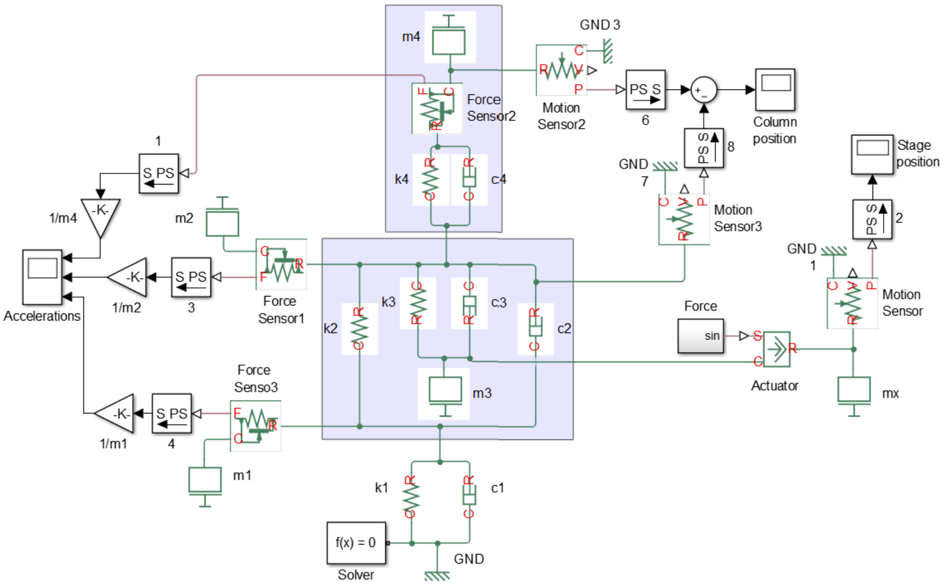

Figure 4.2: 1D lumped mass-spring-damper model of the EBPG in Simscape

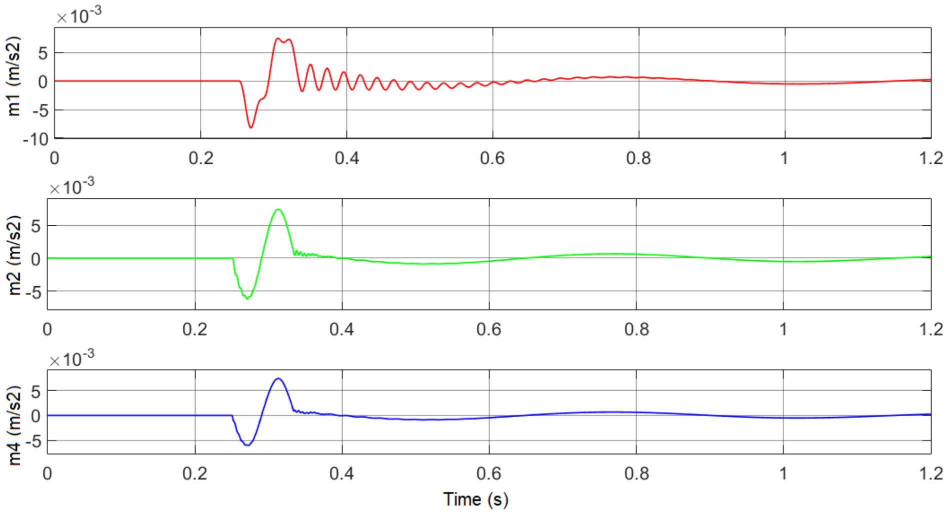

Figure 4.3: Acceleration vs time plot for m_4, m_2, and m_1 in X-direction after stage motion of 1mm

has vibrations for longer period of time and the sytem has a rigid body mode due to oscillation of the damped frame.

The acceleration amplitude and frequency components are not the same. The amplitude can be scaled to the match the experimental data.

5

Concept generation and selection

The solution method has two primary requirements: decrease stage motion time, and decrease beam settling time. This chapter discusses detailed concept generation for several solution methods. In section 5.1 and section 5.2, methods to reduce the e-beam settling time and the stage motion time are discussed respectively. In section 5.3, these solution methods are compared based on three main criteria: effectiveness, implementability and drawbacks. In section 5.4, the individual concepts for both requirements are chosen and their compatibility is discussed. A detailed design of the final solution method is discussed in the next chapter.

5.1. Solutions to reduce the e-beam settling time

The source of the payload-induced error in the e-beam is the oscillations of the EOC. The EOC oscillations are caused by the reaction force generated in the stage assembly, that travels up to the EOC. Therefore, there are three types of possible solutions:

1. **Resolve the reaction force at source** (i.e. stage assembly)
   The reaction force can be neutralized by balancing it with an additional force. However, we can't just use an actuator to apply this additional force. Because the actuator will impart a reaction force on the part it is mounted and it can make the problem worse.

   There are two smart strategies to balance the force. First, to create a counter-force with a modified control strategy. Second, to add additional moving mass generating equal and opposite reaction force on the stage.

2. **Prevent the transmission of the force from the stage to the EOC**
   To prevent transmission of the force to the EOC, either the mechanical connection between the stage and the EOC can be eliminated or these forces can be redirected.

3. **Reduce for the effect of the force**
   To reduce the effect of the reaction force on the e-beam, the EOC can be modified to reduce the oscillations. Also, an additional sensor can be used to measure the EOC vibrations and correct the e-beam in real-time.

These solution methods are discussed in detail in the following subsections.

5.1.1. Input shaping and disturbance rejection

Input shaping or time-delayed filtering is a method where the actuation force is divided into two (or more parts) and these parts cancel the vibrations caused by each other. Basically, creating a signal that neutralizes its own vibrations. Singh et al. [16][15] and Lau et al.[10] have used input shaping to control the flexible systems. To implement input shaping to the stage control, the natural frequency (ω) and damping ratio (ζ) of the EOC must be known.

Based on the EOC properties, the stage actuation signal can be divided into multiple parts with amplitudes A_i starting at time t_i as follows:

$$\begin{bmatrix} A_i \\ t_i \end{bmatrix} = \begin{bmatrix} \frac{1}{1+K} & \frac{K}{1+K} \\ 0 & 0.5T_d \end{bmatrix}$$

Where, $K = exp\left(\frac{-\zeta\pi}{\sqrt{1-\zeta^2}}\right)$ and $T_d = \frac{1}{\omega\sqrt{1-\zeta^2}}$ [15].

An example of input shaping is shown in figure 5.1.

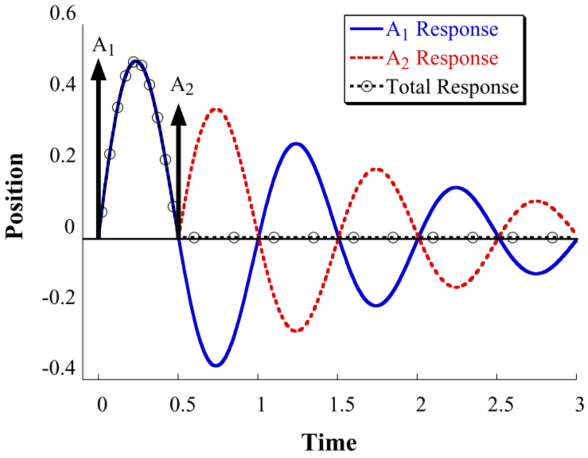

Figure 5.1: Input shaping: actuation signal divided into two parts[15]

There is one other way to resolve the problem at the source. If the natural frequencies of the EOC are known, using a notch filter these frequencies can be removed from the actuation signal. Although it will reduce the EOC oscillations, it will not stop it.

Effectiveness: The EOC has complex dynamics and it can have multiple natural modes. This makes designing an input shaper that doesn't excite any of the EOC modes, a complicated task. However, a simple input shaper should be able to reduce the column oscillations up to an extent. The same is the case with the notch filter, it is also moderately effective.

Implementability: Both input shaper and notch filter can be programmed into the controller without any major changes in the system hardware. However, to tune the input shaper and notch filter, knowledge of system parameters is required. The dynamics of the EOC and the relationship between the EOC and the e-beam error are not completely known. It makes input shaping or disturbance rejection hard to implement.

Drawbacks: By dividing the actuation force, the input shaper makes the stage motion slow.

An additional notch filter in the stage control can adversely affect the stage motion.

5.1.2. Counter mass on the stage

Counter mass is an effective way to balance the reaction force of the stage. The counter mass is an additional body mounted on the same base and moving in the opposite direction. Therefore reaction force due to counter mass will cancel the reaction force of the stage on the base.

Effectiveness: A properly designed counter mass can neutralize the stage reaction force completely.

Implementability: Incorporating an additional body within the volume constraints may require design changes in the current system.

Drawbacks: To actuate the counter mass, additional energy is required.

5.1.3. Inerter for the stage

An inerter is a rotating mass (flywheel) actuated by a linear motion, as shown in figure 5.2. The inerter produces equal and opposite forces proportional to the relative acceleration of its terminals. It behaves

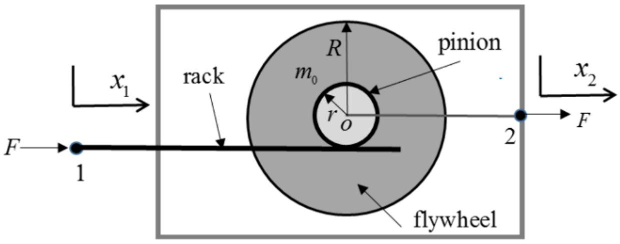

Figure 5.2: Schematic diagram of an inerter [7]

like a mechanical equivalent of a capacitor. Javidialesaadi et al.[7] has used an inerter as a damper for passive structure control.

An inerter can also be used to redirect a force from a moving mass to another stationary mass. By grounding one terminal, the inerter can behave as a virtual counter mass redirecting the forces to the ground. By increasing the ratio of radii of the flywheel (R) and the pinion (r), a high effective mass (m_e) can be created from a lightweight inerter (m_o), as shown below:
The force F needs to satisfy the equilibrium about point O.
Where, $F = m_e(x''_2 - x''_1) = T/r$, $T = J\theta''$ and $J = \frac{1}{2}m_o R^2$

$$\Longrightarrow\ m_e = m_o\left(\frac{R}{r_o}\right)^2$$

An inerter can be used to redirect the reaction force of the stage. However, the force can not be transmitted to the ground as a rigid ground connection is not possible. Otherwise, ground vibration will be transmitted to the system. Therefore, the inerter has to be connected somewhere in the system.

Effectiveness: An inerter can only redirect the reaction force. It can not balance the reaction force. By redirecting the force outside of the exposure chamber to a heavy mass such as the crane, the effect can be reduced.

Implementability: The inerter needs a rigid connection passing through the exposure chamber wall. Steps have to be taken to keep the exposure chamber vacuum sealed. Furthermore, the inerter for the Y-stage can be connected to the motor mounted on the stationary plate. However, the motor for X-stage is mounted on the Y-stage which itself is not stationary. This makes the implementation of an inerter for X-stage highly complex.

Drawbacks: The inerter connects the stage with the outside world, this can result in external force transmission to the stage. It also makes disassembling the stage complicated, thus reducing the maintainability of the EBPG.

5.1.4. Counter mass outside of the Exposure chamber

Volume constraint can prevent the implementation of a counter mass in the exposure chamber. To avoid this constraint, the counter mass can be installed outside of the exposure chamber connected to the vacuum cover as shown in figure 5.3(a). The counter mass can be tuned to counter the oscillations of the vacuum cover, reducing the transmission of the reaction to the EOC.

The counter mass can balance the reaction force on the vacuum cover but both forces are not planar and it will generate a torque on the system. This torque can deform the system and will cause vibrations in the system. However, the counter mass can be installed in the same plane parallel to the stage, mounted on the outer surface of the exposure chamber walls. This way the torque generation can be avoided but the finite stiffness of the exposure chamber makes the counter-mass less effective.

Effectiveness: Counter mass installed on a different body than the stage mounting is moderately effective.

Implementability: The counter mass needs additional actuators. The magnetic fields of the actuator placed on the vacuum cover or anywhere near the EOC can interfere with the e-beam. Placing the counter mass on the side plates require additional stiffness. Thus making it less implementable.

Drawbacks: The counter mass needs additional actuators and energy. And generated torque adversely affects the system dynamics.

Figure 5.3: (a)EBPG with a counter mass on the vacuum cover. The Red arrows represent the reaction forces of stage motion and counter mass motion. The green arrow represents the resulting torque.(b) EBPG with detached EOC and stage.

5.1.5. Detach stage from the EOC

The force loop can be rerouted to remove the EOC from the force loop. It can be achieved by detaching the stage and mounting it on a separate frame. A schematic for a simple redesign to detach the subsystems is shown in figure 5.3(b).

Effectiveness: Detaching the EOC and stage can stop the transmission of the force to the EOC. This makes the EOC oscillations obsolete, resulting in zero settling time for the e-beam.

Implementability: A continuous vacuum has to be maintained between the EOC and the exposure chamber. Therefore, a flexible connection between the two subsystems is required. Mounting the stage on a separate frame can also make it difficult to keep the optical height fixed. Both frames have to be synchronized in the Z-direction.

Drawbacks: Detaching the EOC and the stage makes needs a complete redesign, making the design undesirably complex and also reduce the transportability of the EBPG. And if two frames are not completely synchronized, vertical position fidelity between column and substrate will be affected adversely.

5.1.6. System rearrangement

In the current design, the center of gravity (CoG) of the system lies above the damped frame and center of rotation for rigid body mode lies on the damped frame. This makes the system less stable. Any rigid body rotation will move the CoG lower thus requiring more force from the dampers to counter the rotation. This result in less effective damped frame. The system can be redesigned to move the damped frame above the CoG.

Effectiveness: Moving the damped frame above the CoG can make the system more stable. This can not only help in damping the rigid body mode but also to damp the EOC oscillations. However, the air dampers are not designed to damp high-frequency internal vibrations.

Implementability: It needs substantial design change to rearrange the subsystems.

Drawbacks: System redesign can reduce transportability.

5.1.7. Sensor on the EOC

An additional sensor can be used to measure the oscillations of the EOC. This measurement can be used to compensate for the e-beam error.

Effectiveness: If a direct relation can be found between the EOC oscillations and the e-beam error, the e-beam can be corrected in real-time.

Implementability: Since the relationship between the EOC oscillations and the e-beam error is not completely known, it is difficult to implement this strategy.

Drawbacks: This strategy has no apparent drawbacks.

5.1.8. Stiffer EOC

To reduce the oscillations and increase the natural frequency of the EOC, it can be made stiffer.

Effectiveness: A stiffer EOC will have oscillations with smaller amplitude.

Implementability: It is not completely known that what natural modes of the EOC are to be avoided to reduce the effect on the e-beam. The EOC has a complex architecture and increasing the stiffness requires proper knowledge of the dynamics.

Drawbacks: With the increase in the stiffness, mass can increase as well. And with increase in mass natural frequency will come down as well ($f = \sqrt{\frac{k}{m}}$).

5.1.9. Damper on the EOC

To damp the EOC oscillations quicker, additional tuned mass dampers can be mounted on the EOC.

Effectiveness: The dampers can reduce the settling time of the column. (*Appendix D.2*)

Implementability: To mount tuned mass dampers on the EOC, system dynamics and important modes should be known. Also, it is not clear which column modes are to be avoided because the EOC and the e-beam has different excited frequncies due to the stage motion.

Drawbacks: Adding tuned mass dampers can slightly increase the system weight.

5.2. Solutions to reduce the stage motion time

There are several strategies to make the stage faster. These strategies are discussed in the following subsections.

5.2.1. Increase acceleration and velocity limits

The simplest way to make the stage faster is to increase the acceleration and velocity limits. **Effectiveness:** With higher limits of the acceleration and the velocity, the stage motion time will be reduced.

Implementability: The increased limits might not be achievable with the available controller and electronics such as voltage supply, amplifier and motor may need upgrading.

Drawbacks: Higher stage acceleration will cause a larger reaction force. It will make the EOC oscillations worse, resulting in a longer settling time.

5.2.2. Fourth order trajectories

The sinusoidal trajectory doesn't have a constant acceleration phase. And the rate of change of acceleration can not be varied. Lambrechts et al.[9] have developed an algorithm to generate time optimal fourth order trajectories for stage motion. A fourth-order trajectory gives the user complete control over trajectory parameters. It has a constant acceleration phase which helps in reaching the velocity limit quickly. Figure 5.4 shows plots for a typical fourth-order trajectory.

Effectiveness: Fourth order trajectory can reduce the stage motion time up to an extent, keeping the acceleration and velocity limits the same.

Implementability: A fourth-order trajectory generation requires limits for snap and jerk. The trajectory generation involves numerical integration multiple times.

Drawbacks: Actuation force of a fourth-order trajectory consist of multiple frequency components. Unlike sinusoidal trajectory, where actuation force has a single frequency. The fourth-order trajectory can excite multiple system modes simultaneously, also gives you two frequencies that are avoided

5.2.3. Stage mass reduction

A lighter stage can move faster with the same actuation force. To make the stage substantially fast, a large portion of material from the stage has to be reduced. Reducing material from the stage can reduce the stage stiffness as well. To maintain the stiffness and reduce the mass, topology optimisation can be used.

Effectiveness: Stage mass can not be reduced significantly without negatively affecting the stage stiffness. Hence, this strategy is only moderately effective.

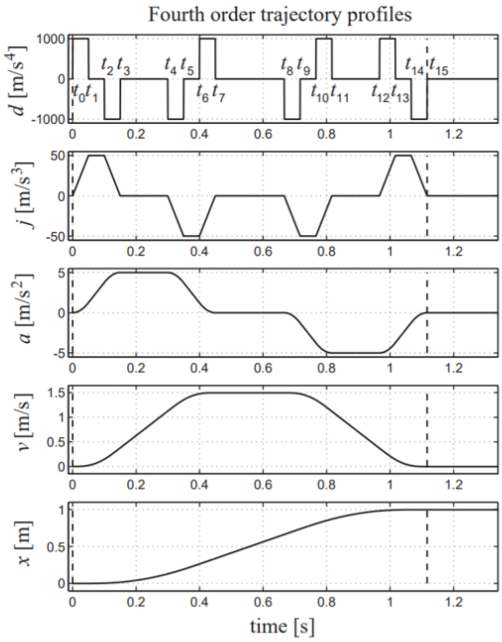

Figure 5.4: Snap, jerk, acceleration, velocity, and position plots for a typical fourth order trajectory[9]

Implementability: Topology optimization is requires computing power to design and complicated techniques to manufacture. This makes mass reduction an expensive process.

Drawbacks: Decreasing the stage mass can reduce the stiffness. And topology optimization can create air pockets in the stage, thus making it incompatible with the vacuum.

5.3. Comparison

A Harris profile is created to compare the discussed strategies as shown in figure 5.5. The strategies are compared for effectiveness, implimentability and drawbacks of the method. The effectiveness and implimentability are graded on a scale of 1 to 5, where 5 is the best and 1 being the worst. Drawbacks are graded on a negative scale from -1 to -5, where -1 being the best and -5 being the worst. All three criteria are equally important and weighted equally. A sum of all three grades for a criterion gives a quantitative value for suitability.

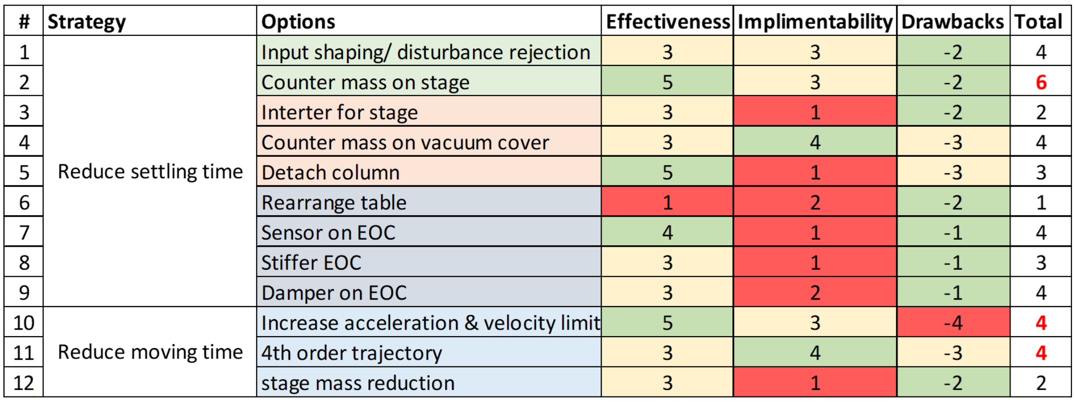

#	Strategy	Options	Effectiveness	Implimentability	Drawbacks	Total
1	Reduce settling time	Input shaping/ disturbance rejection	3	3	-2	4
2		Counter mass on stage	5	3	-2	6
3		Interter for stage	3	1	-2	2
4		Counter mass on vacuum cover	3	4	-3	4
5		Detach column	5	1	-3	3
6		Rearrange table	1	2	-2	1
7		Sensor on EOC	4	1	-1	4
8		Stiffer EOC	3	1	-1	3
9		Damper on EOC	3	2	-1	4
10	Reduce moving time	Increase acceleration & velocity limit	5	3	-4	4
11		4th order trajectory	3	4	-3	4
12		stage mass reduction	3	1	-2	2

Figure 5.5: Harris profile

Harris profile has a severe disadvantage, user bias. Assigning numerical value to a criterion can be influenced by the user's prejudice. To avoid user bias, the profile is extensively discussed with colleagues and fellow students.

5.4. Concept selection

According to the Harris profile, stage counter mass is the most suitable method to reduce the e-beam settling time. The stage with a counter mass doesn't apply any reaction force on the system, therefore the actuation force can be increased without affecting the settling time.

To reduce stage motion time, increasing the acceleration and velocity limits and implementing fourth-order trajectory, both are equally suitable. Furthermore, both strategies can be implemented simultaneously.

It can be inferred that mentioned three strategies are compatible with each other. Hence, **final solution method is a combination of three strategies, stage counter mass, higher acceleration-velocity limits, and fourth-order trajectories**.

6

Detailed concept design

To increase the system throughput, a solution method that is a combination of three strategies (stage counter mass, higher accelerationvelocity limits, and fourth-order trajectories) is proposed. In this chapter, a detailed concept design is discussed. The solution method is developed in multiple steps. First, in section 6.1, a stage counter mass is designed. Followed by the development of a fourth-order trajectory generator in section 6.2. In section 6.3, simulation results are discussed.

6.1. Counter mass design

A counter mass has to be designed that can be integrated into the current system without violating the mechanical constraints. The counter mass should comply with the following guidelines:

- Reaction force of the counter mass should be equal to the reaction force of the stage.
- The plane of motion of the counter mass should be the same as the horizontal plane of motion of the stage.

The reaction force of the stage is **stage mass** × **acceleration**. To generate equal reaction force, the product of the mass and acceleration of counter mass should be equal. Considering the volume constraint, a smaller counter mass with higher acceleration can be used. A smaller counter mass will also have a bigger stroke length, hence it will end up needing more space. Not only that, to provide different acceleration to the counter mass than the stage, either an additional actuator is required or a gearbox is required. An additional actuator needs more space and generates heat and magnetic fields that have to be taken care of. So it is not advisable to increase the number of actuators inside the exposure chamber. Therefore a counter mass with the same mass as the stage is deemed suitable.

It is observed that counter mass and the stage can not exist in the same horizontal plane due to space constraints. So the next best thing is to have their centre of mass close to each.

Studying the CAD model of the stage assembly, it is noticed that a counter mass for X-stage can be added in the space between X-plate and Y-plate. The available space is shown in figure 6.1.

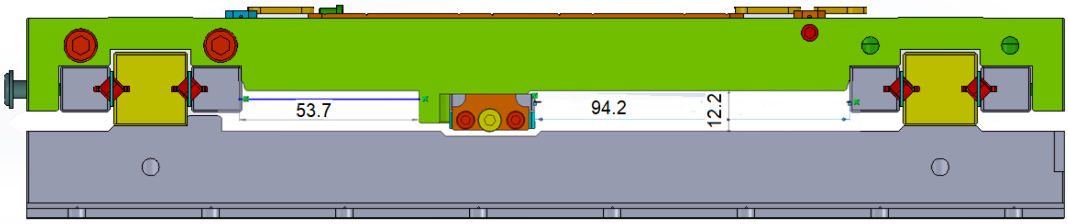

Figure 6.1: Space available between X-plate and Y-plate (Dimensions are in mm).

Assuming the counter mass can have same width as the X-plate (310 mm), length (53.7 + 94.2) and height 12.2 mm, the available area is **45.8** × **10**^{3} **mm**^{2} and available volume is **55.9**× **10**^{4} **mm**^{3}.

Assuming the counter mass is made of Tungsten since it has high density (ρ = 19.3 g/cm^3), the volume for same mass as the X stage (11.6 kg) will be **60.1×10^4 mm^3**. This volume is larger than the available volume.

It is observed in the stage assembly in figure 6.2, that space underneath the stage can be reduced by replacing the Z-stage with a smaller actuator. By moving the Y-plate and stationary plate down, space can be made for the counter mass while keeping the same optical working distance. Therefore, the Z-stage is reduced 10 mm in height and space between X-plate and Y-plate is increased.

Figure 6.2: Cross section view of stage suspension

Material selection: Tungsten has a different thermal expansion coefficient than the stage (AMC) and also low machinability. Therefore, a bi-material counter mass is proposed, where tungsten blocks are mounted on the base plate made of AMC to match thermal expansion. And both the materials are vacuum compatible.

Actuator: Since the counter mass is mounted just below the stage, the actuator for the X-stage can be used to move the counter mass as well. A rack can be added on the counter mass opposite to the rack mounted on the X-stage. This way the same motor can actuate both the masses and reaction forces on the pinion will cancel each.

Bearing selection: To mount the counter mass such that it has one degree of freedom, linear bearings can be used. The linear bearings must have a stroke length equal to the stage stroke (210 mm), a load capacity of at least 150N and they should be vacuum compatible. The model RNG6300x28KRE bearing from PM B.V. fulfils all the requirements (as shown in table 6.1) and it's also equipped with an anti-creep cage making the bearing suitable for long term use.

Table 6.1: RNG6300x28KRE bearing properties

Parameter	**Value**
Stroke length	210 mm[1]
Load capacity	57415 N
Vacuum compatibility	Yes, alll metal design
Anti-creep cage	Available

6.1.1. CAD and FEA

The counter mass is designed with an AMC base plate, two tungsten blocks, two bearings and a rack of a total mass of 11.6kg. The exploded counter mass is shown in figure 6.3.

---

[1] Out of the box stroke length is 200 mm which can be increased by 10 mm by reducing the cage length

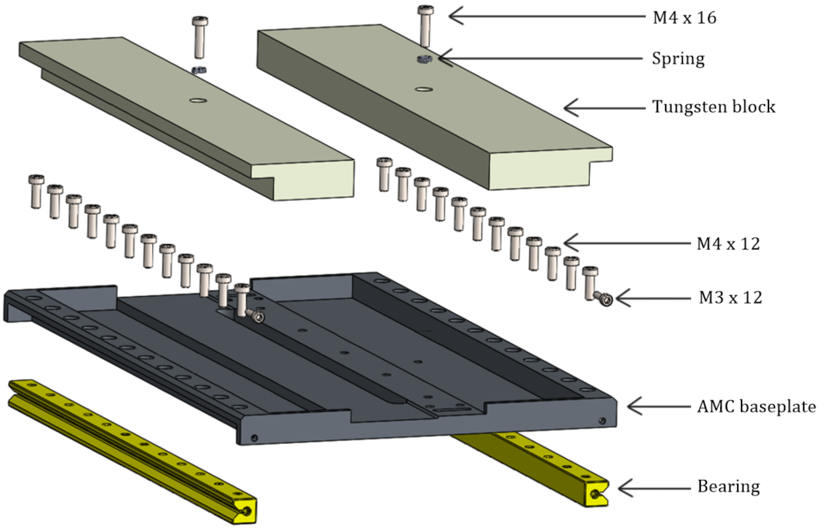

Figure 6.3: Exploded view of the counter mass for X-stage

Tungsten blocks are mounted with a spring-loaded bolt in the middle. The bolt coincides with the thermal centre and the block can expand around it. The spring helps tune the friction such that it allows for the block to expand due to thermal changes. But the friction restricts the relative motion between the block and the base plate during the counter mass motion (*Appendix D.3*)

The bearings are constrained using multiple M4 bolts from the top and one M3 bolt from the side. The holes in the base plate for the M4 bolts are larger in diameter. This helps avoid the problems due to over constraints during assembly. The M4 bolts are loosely fitted and the only constraint in the vertical direction. The M3 bolt from the side push the bearing in X-direction and provides the next constraint. The bearings are pushed inside with their counterparts mounted on the Y-plate in Y-direction. Finally, the M4 bolts on the counter mass can be tightened. The counterparts of the bearings have two push bolts in Y-direction to pretension the counter mass. An exploded view of the stage assembly with the counter mass is shown in figure 6.4.

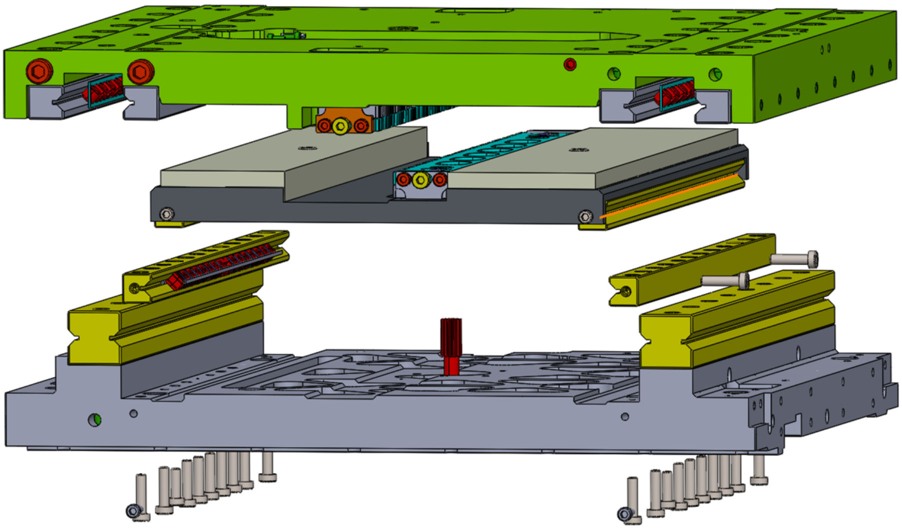

Figure 6.4: Exploded view of the stage assembly

FEA of the counter mass: A finite element analysis is done for the base plate. The plate is constrained from the surface that is supposed to be supported by the bearing. Furthermore, tungsten blocks weight and gravity are applied. It was observed during the FEA, that the base plate has less stiffness in between the tungsten blocks. To increase the stiffness to mass ratio, ribs were added on the side and in the middle passing across the base plate. Further study revealed that the middle rib doesn't help significantly with the stiffness and is removed (*Appendix D.1*).

The FEA results for the final design are shown in figure 6.5. The base plate has the highest stress of 1.8 MPa and maximum deformation of 6 μm downwards. And the first natural frequency is 622 Hz. The yield strength for AMC is 380MPa. All values are well within acceptable limits.

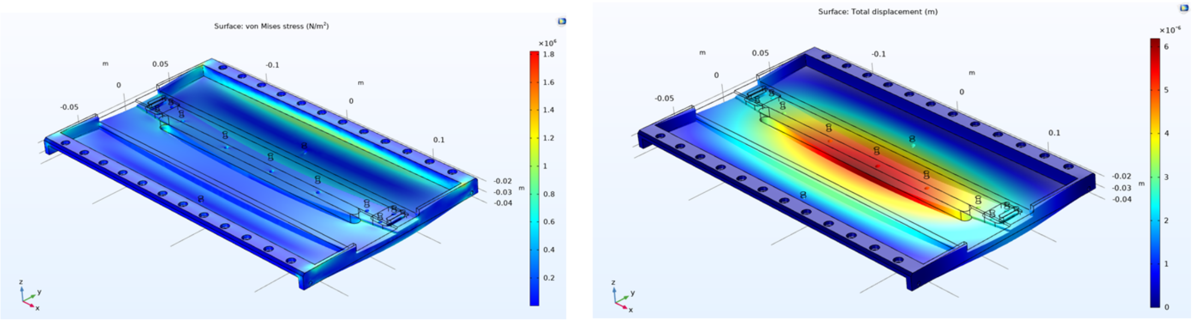

(a) (b)

Figure 6.5: Finite element analysis of the base plate, (a) Stress plot, (b) Deformation plot

An FEA thermal analysis is conducted to study the feasibility of bimetallic counter mass. For the temperature change of 1°C during the operation (20°C), maximum thermal stress is 7MPa and maximum deformation is 8.5 μm (figure 6.6. Both values are well in the acceptable range. For the temperature change of ±5°C during transport, the maximum thermal stress is 35MPa and it also does not cause any plastic deformation. This makes the design thermally acceptable.

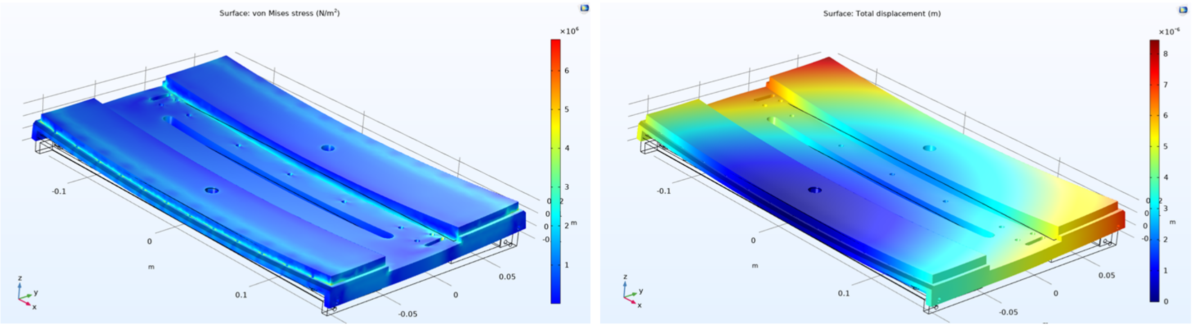

(a) (b)

Figure 6.6: Thermal analysis of counter mass for temperature range 19-21°C, (a) Stress plot, (b) Deformation plot

Feasibility study for the actuator and pinion: The motor in the proposed design has to provide the torque for the stage and the counter mass. The BLDC motor is able to provide 129mNm nominal constant torque. And for the current pinion radius of 3.75 mm, the motor can provide maximum force of 34.4N. To actuate both the X-stage and the counter mass ($m_{total} = 2 \times mx = 23.2kg$), a maximum acceleration of $(34.4/23.2 =)$ **1.48 m/s**^{2} can be achieved.

This increased torque is transmitted via the pinion. Therefore, the pinion shaft has to be able to withstand the torque. The pinion shaft is made of X90CrMoV18 steel with endurance limit of 144MPa and the motor stall torque is 370mNm. For the torque (T) of 370mNm, maximum torsional stress is calculated below:
Torsional stress, $\tau = \frac{T.r}{J} = 8.74\text{MPa}$,

where r is the radius of the pinion shaft (3mm) and J is polar moment of inertia ($J = \frac{\pi.r^4}{2} = 127mm^4$). Therefore, the pinion shaft has a **safety factor** of $(144/8.74 =)$ **16.48**.

The addition of counter mass does not affect the force on the gear teeth, as different teeth are engaged with the stage rack and the counter mass rack. The pinion in the current system is designed for a force of 55N[2]. And even for the increased acceleration(maximum force of 34.4N), the pinion design is acceptable.

6.2. Trajectory generator

Fourth-order trajectory generator:

A fourth-order trajectory generator is developed using the equations from ”Trajectory planning and feedforward design for electromechanical motion systems”[9]. The fourth-order trajectory generator requires limits of snap, jerk, acceleration and velocity to generate the trajectory setpoints. The snap and jerk limits depend on the control electronics (voltage limits and controller bandwidth). To be on the safe side, the limits measured from the sinusoidal trajectories are used (*Appendix B.1.2*), i.e. maximum snap = $3 \times 10^7 m/s^4$ and maximum jerk = $1.5 \times 10^5 m/s^3$.

A comparative study is conducted between the sinusoidal trajectory and fourth-order trajectory for the current acceleration (0.9 m/s^2) and velocity (0.04 m/s) limits as shown in figure 6.7.a and percent advantage is plotted in figure 6.7.b. The percent advantage is defined as

$$\text{Percent advantage} = \frac{T_{sin} - T_{4th}}{T_{sin}} \times 100$$

where, T_{sin} is stage motion time for sinusoidal trajectory and T_{4th} is stage motion time for fourth-order trajectory for a given step size.

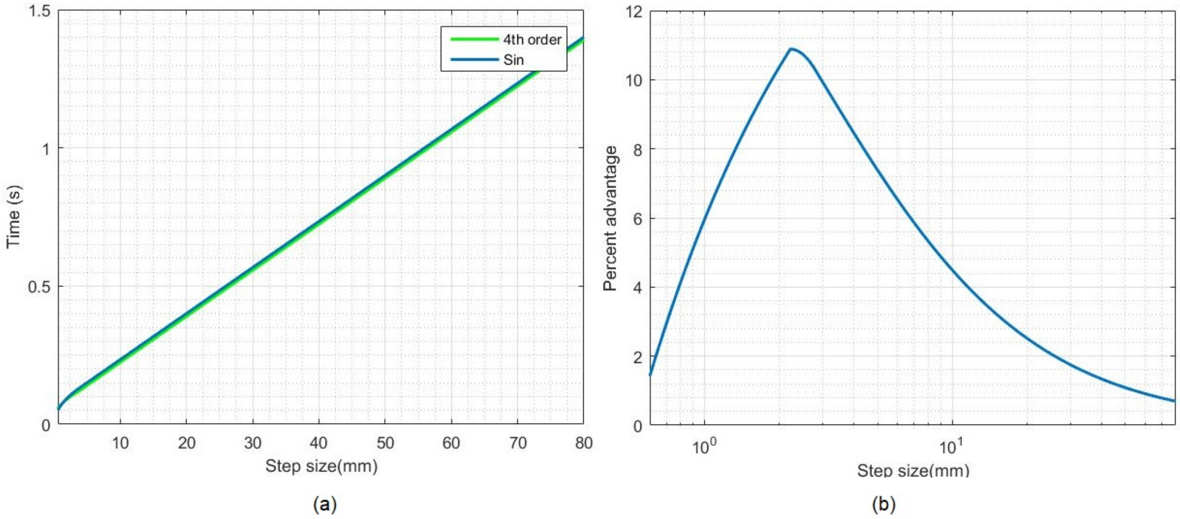

Figure 6.7: Sinusoidal vs fourth-order trajectory(a) Stage motion time comparison (Blue line represents sinusoidal trajectory and Green line represents fourth-order trajectory) (b) Percent advantage

Acceleration and velocity limits:

Using the Simulink model, the effect of the increase in acceleration and velocity limits for a sinusoidal trajectory is studied. It can be observed in the figure 6.8 that higher acceleration limits can reduce the stage motion time for smaller steps, but have less effect for the larger steps. Whereas, increased velocity limits have no effect on the stage motion time for smaller steps (as the velocity doesn’t reach its limit), but can reduce the stage motion time significantly for larger steps. Therefore a combination of two should be implemented. The acceleration limit of 1.4 m/s^2 and velocity limit of 0.06 m/s is chosen. These values are later used in the fourth-order trajectory generator.

6.3. Simulations

6.3.1. Mass sensitivity for the counter mass

The Simulink model is used to simulate the X-stage counter mass on the system as shown in figure 6.9. It has been observed that for the ideal system, there are no oscillations in the EOC due to the stage motion for a system equipped with a counter mass. However, the stage mass can vary up to ±250g

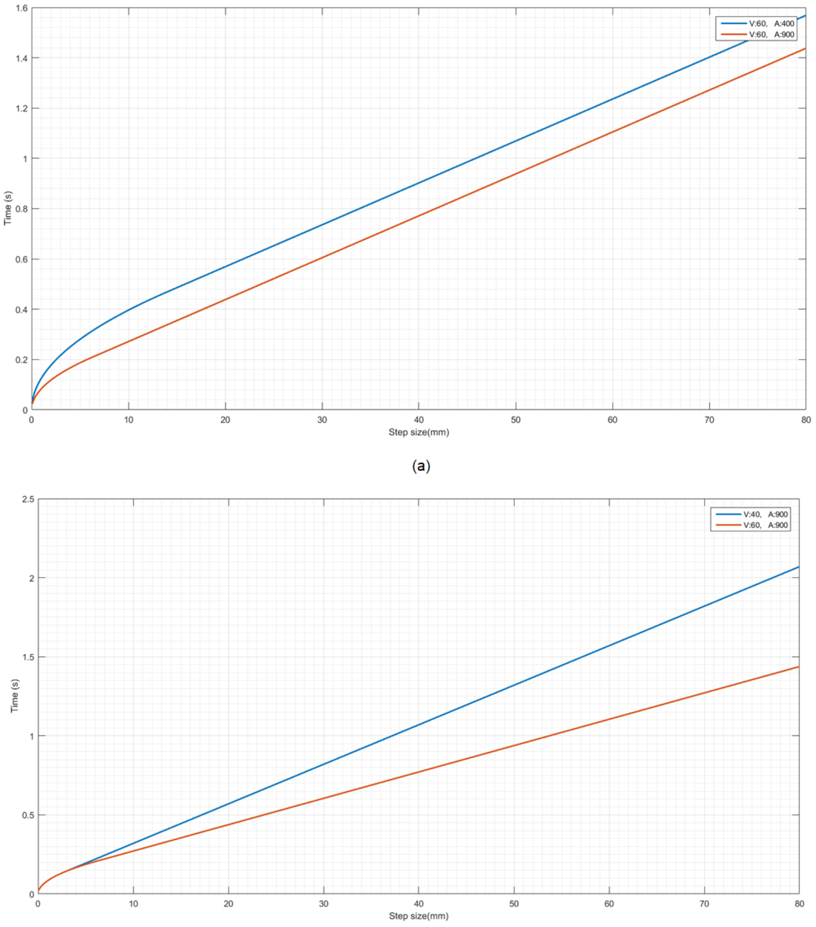

(a)

(b)

Figure 6.8: Stage motion time vs step plots (a) Acceleration comparison (Blue line represents acceleration limit=0.4 m/s^2 and Red line represents acceleration limit=0.9 m/s^2) (b) Velocity comparison (Blue line represents acceleration limit=0.04 m/s and Red line represents acceleration limit=0.06 m/s)

for different substrates. The model is simulated to see the effect of the mass difference between the X-stage and the counter mass. The sensitivity function for stage mass is derived,

Acceleration amplitude = 0.0028 (stage mass variation) m/s^2.

where stage mass variation is in kg.

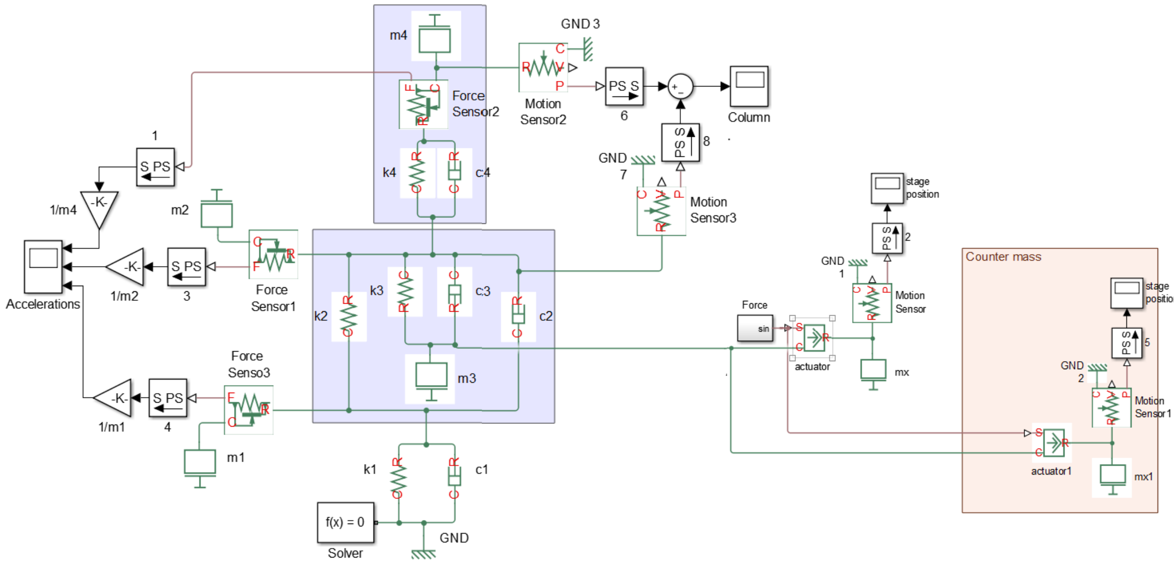

Figure 6.9: Simulink model for the EBPG with counter mass

The acceleration plots for the system without the counter mass and with the counter mass having 250g mass difference are shown in figure 6.10. It can be observed that even if there is a 250g mass difference between the counter mass and the X-stage, the vibration amplitude for the EOC is ~50 times smaller than without a counter mass.

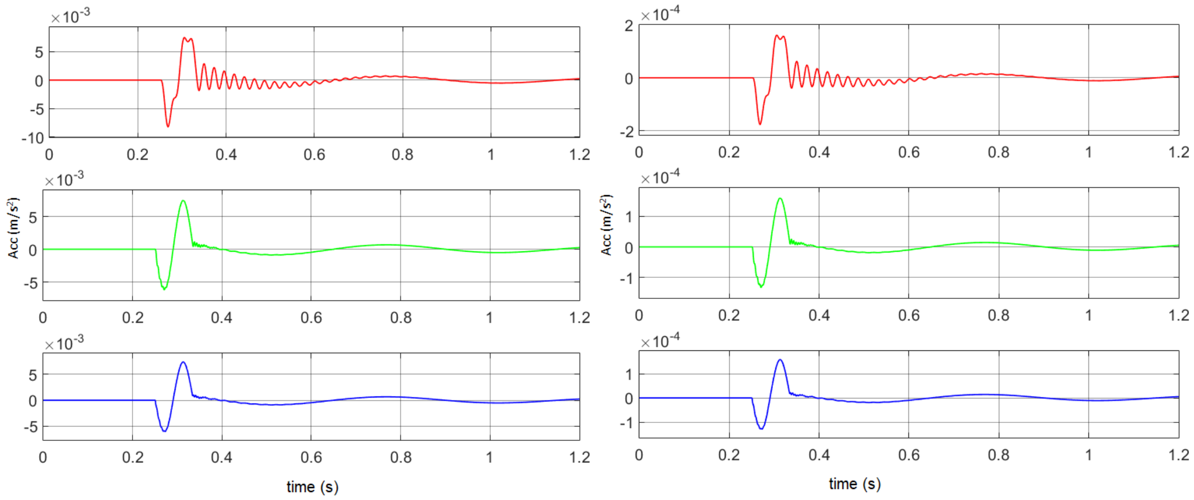

(a)

(b)

Figure 6.10: Acceleration vs time plots for simulink model after step of 1mm (a) No counter mass (b) counter mass with 250g mass difference

Assuming the amplitudes of vibrations for the EBPG and the model can be linearly scaled, the counter mass will reduce the EOC acceleration amplitude by 50 times. Also, the position error plots for the EOC are plotted in figure 6.11. The amplitude of position error is also smaller by 50 times for a system equipped with a counter mass. Recalling from the experiments, the amplitude of the e-beam error was also proportional to the amplitude of the EOC vibrations. Therefore the counter mass should also reduce the e-beam error by 50 times. The highest amplitude of the payload-induced error in the e-beam is 15nm and the 50 times reduction makes the payload-induced error to be in the acceptable range and reduce the settling time to zero.

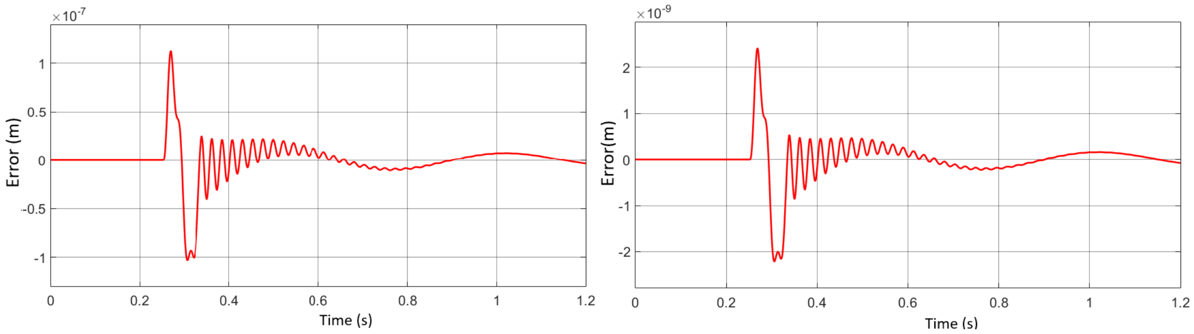

(a) (b)

Figure 6.11: Position vs time plots for the EOC after step of 1mm (a) No counter mass (b) counter mass with 250g mass difference

6.3.2. Effect of X-stage counter mass on Y-stage

The x-stage counter mass solves the settling time problem for the X-motion but it makes the Y-motion worse. Since the Y-stage has to carry X-stage and the counter mass with it, the reaction forces due to Y-motion will increase. Another simulation is performed for the Y-stage motion which shows that amplitudes of Y-direction accelerations increase 60% due to the X-counter mass.

6.3.3. Stage motion time

The stage motion time plots are plotted to study the improvement due to the proposed trajectory generator. The plots are shown in figure 6.12. It can be observed from the plots that the new trajectory can reduce the stage motion time by ~20% for smaller steps and up to 32% for larger steps. For step size smaller than 3 mm, the new acceleration trajectory has constant acceleration phase for very short period of time and velocity doesn't reach the limit. It's because the jerk limit constraints the acceleration slop, therefore it takes longer to reach the acceleration limits and allows little time for constant acceleration phase. For larger steps, velocity limit is not only reached but the trajectory also has a constant velocity phase. The stage can be made faster for smaller steps by increasing the limits of acceleration, jerk and snap.

For the new trajectory generator, the stage motion time for the 1mm step is 67 ms and for the 80mm step, the stage motion time is 1.4 s. For smaller

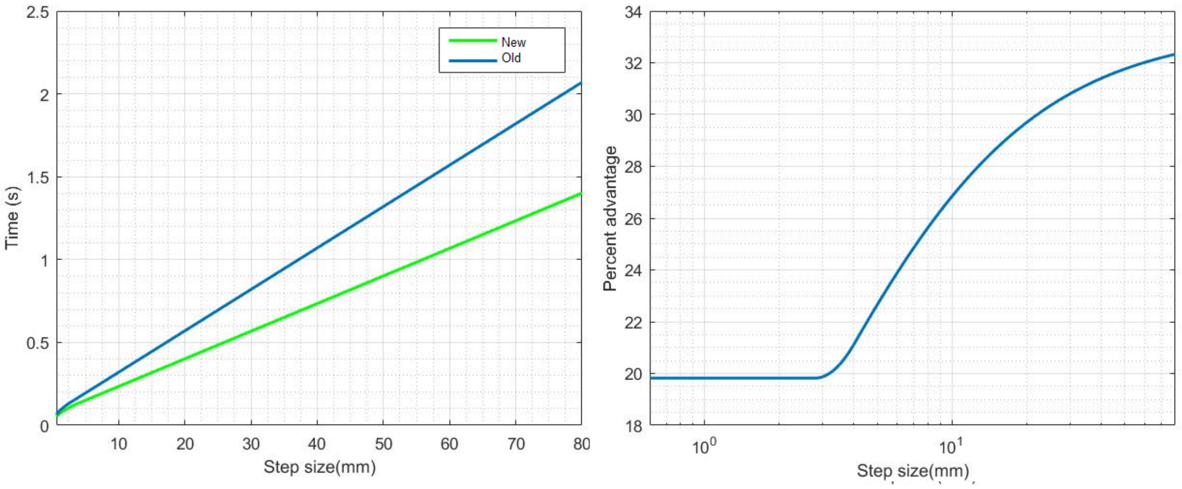

(a) (b)

Figure 6.12: Sinusoidal vs fourth-order trajectory(a) Stage motion time comparison (Blue line represents old trajectory and Green line represents proposed trajectory) (b) Percent advantage

6.4. Results

- The x-counter mass reduces the beam settling time to zero, even with the 250g mass difference between the X-stage and the counter mass.
- The X-counter mass increase the mass of the Y-stage by 11.6kg. And increase the acceleration amplitude of the EOC by 60%.
- The new trajectory generator can reduce the stage motion time by 20% for the small steps and up to 32% for larger steps.
- The new stage settling time for the 1 mm step in X-direction is 67 ms compared to original stage settling time of 186.3 ms. That is 64% reduction.
- The new stage settling time for the 80 mm step in X-direction is 1.4 s compared to original stage settling time of 2.17 s. That is 35% reduction.

7

Conclusion and recommendations

7.1. Conclusion

The aim of this project was to increase the throughput of the EBPG by improving the dynamics. By conducting an extensive system evaluation, it was found that system dynamics play the biggest role during the exposure of sparse patterns. The most time-consuming steps during a sparse pattern exposure are stage motion and e-beam settling. Both steps have a causal relationship, the stage motion creates a reaction force that is responsible for the EOC vibrations. And the EOC vibrations cause the e-beam error. A new parameter is defined to observe the combined effect of the stage motion and beam settling, named **stage settling time**. It was observed that the X-stage moves more frequently than the Y-stage, therefore this project was aimed to reduce the stage settling time for the X-stage. The proposed solution consists of a counter mass for the X-stage and a fourth-order trajectory generator. The counter mass cancels the reaction force of the X-stage and the new trajectory generator makes the stage faster. The proposed solution method reduces the beam settling time to zero and the stage motion time by at least 20%. For 1mm step the stage settling time is reduced by 64% and for 80mm step the stage time is reduced by 35%. The solution method improves the X-direction motion but deteriorates the Y-direction motion. However, the overall effect of the solution is positive, considering the Y-direction motion is less frequent.

7.2. Recommendations

- In the new trajectory generator the acceleration is limited by the motor and other higher order derivatives (snap and jerk) are limited by the controller electronics. By improving the controller, stage motion time can be reduced further.
- The relation between the EOC and the e-beam is not completely known. By conducting further experiments the relationship can be determined. A simple experiment is to attach multiple sensors (accelerometers) on various locations on the EOC and map the modes and ralation of the column modes to the e-beam. This can help in improving the column architecture.
- To improve the Y-direction motion, a tuned mass damper can be used on the EOC. A simple passive tuned mass damper can be designed by attaching a lightweight mass to the EOC by a spring, tuned to the eigen frequency of the EOC and submerged in a viscous fluid. The mass will vibrate with the EOC and it will take the energy from the EOC. Then the energy will be dissipated due to viscous loss. The tuned mass damper can reduce the beam settling time by a great margin.

A

Material properties

	AISI108	**AMC**	**Zerodur**	**Invar36**	**AISI316**	**AA7075**	**Tungsten**
Density [kg/m3]	7800	2700	2530	8050	8000	**2850**	**19300**
Thermal coductivity [W/mK]	45	141	1.45	10.15	16.3	150	163.3
Thermal exp. coefficient [μm/mK]	12.6	**17.1**	**0.02**	**1.2**	**16.6**	23	4.4
Young's modulus [GPa]	**200**	94	90.3	141	193	70	400
Specific modulus [$10^6 m^2/s^2$]	25.6	**34.8**	35.7	17.5	24	24.6	20.7
Yield strength [MPa]	350	380	-	276	290	390	750

- Steel (AISI108) has high Young's modulus but also low specific modulus. It is used for stationary parts requiring high stiffness (used for Exposure chamber walls).
- AMC has high specific modulus. It is used where less mass is required (used for X and Y stage).
- Zerodur has exceptionally low thermal expansion coefficient and it is used for superplate to keep the effect of thermal changes to a minimum.
- Invar36 also has a low thermal expansion coefficient and it also has a high Young's modulus.
- AISI316 has similar thermal expansion coefficients to AMC and has a high Young's modulus. However, it also has a high density so only used for the stationary plate in stage assembly.
- Aluminium 7075 (AA7075) has low density hence it is used for suspension sidewalls.
- Tungsten has a very high density. But its machinability is low.

B

Stage motion

B.1. Trajectory time and plots

B.1.1. Step time

Using the experiment, the time required for various step sizes in both X and Y directions are measured and listed in table B.1.

Step size	**Time**
X-direction	
- mm	- s
- mm	- s
- mm	- s
- mm	- s
Y-direction	
- mm	- s
- mm	- s
- mm	- s
- mm	- s

Table B.1: Time required for various step sizes

B.1.2. Acceleration, jerk and snap calculation

The trajectory data is used to calculate the limits for acceleration, jerk, and snap.

The trajectory limits are checked for 2 types of steps, long (80 mm) and short (0.25 mm). The available experimental data are position and velocity. The acceleration, jerk and snap data is calculated by differentiating available data (position and velocity). Figure B.1 shows plots for 80 mm steps and figure B.2 shows plots for 0.25 mm steps. The data verifies the velocity and acceleration limits, 40 mm/s and 900 mm/s2 respectively.

For 80 mm step, max jerk value is $5x10^4$ m/s^3 and max snap value is $5x10^6$ m/s^4.

For 0.25 mm step, max jerk value is $1.5x10^5$ m/s^3 and max snap value is $3x10^7$ m/s^4.

It can be inferred that jerk and snap are higher for smaller steps, because in sinusoidal trajectory smaller steps doesn't reach acceleration limit and has steep acceleration profile.

B.1.3. Stage position and settling

Figure B.3 shows the stage position and error plot for a step of 250 μm in X-direction.

B.2. Bode plot for Y-stage

Figure B.6b shows the bode plot for Y-stage. The bandwidth for Y-stage is 28 Hz.

Figure B.1: Trajectory plots for 80 mm step in +X-direction

Figure B.4: Bode plot for the transfer function between the Y stage position and force

Figure B.2: Trajectory plots for 0.25 mm step in +X-direction

Figure B.3: Stage relative position and position error plot for 250 μm in X-direction after the stage is in window

B.3. Ground vibrations

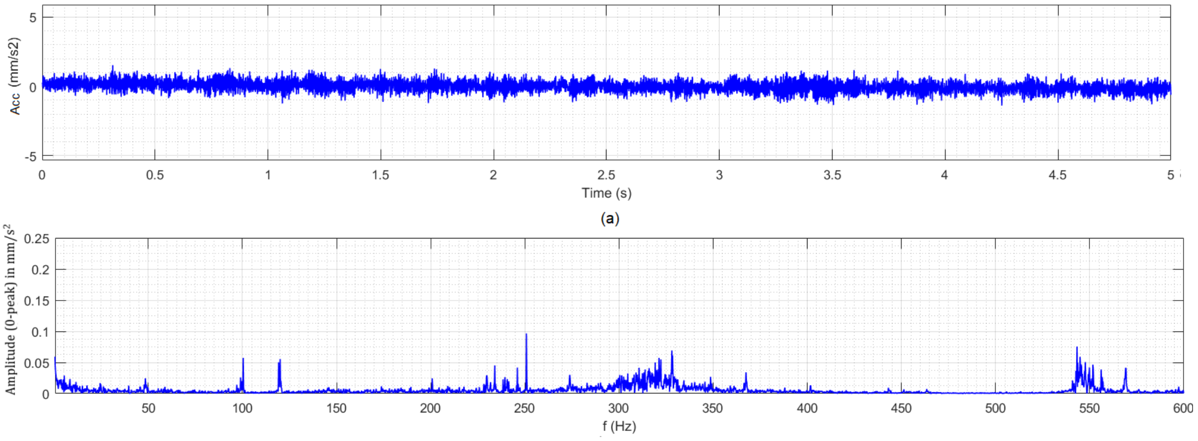

(a)

(b)

Figure B.5: Ground vibrations: (a) Acceleration vs time plot,(b) frequency components

B.4. Beam-on-Edge Plots: X vs Y

Beam error plot for stage motion in X-direction is plotted in figure B.6a and Y-direction is plotted in figure B.6b.

(a) Step of 250 μm in X direction

(b) Step of 250 μm in Y direction

Figure B.6: Beam error v/s time plot

Figure B.7a and B.7b shows the comparison between frequency components of beam error before and after the stage motion of 0.25 mm in X-direction and Y-direction respectively.

Due to the stage motion in X-direction, the excitation frequency bands are 60 Hz and 250 Hz. These are different from excitation due to Y step that are around 32 Hz, 64 Hz, and 80 Hz.

B.5. Effect of X motion in Y direction and Y motion in X direction

It has been observed that for small steps the X-step doesn't create vibrations in Y-direction and vice versa.

However for longer steps (50 mm here), the stage motion in the X-direction cause vibrations on the damped frame in Y-direction. And the step in Y-direction creates vibrations in both directions X and Y at all three positions. However, there are no residual vibrations in the X-direction after the stage finishes the step in Y-direction

(a) Step of 250 μm in X direction.

(b) Step of 250 μm in Y direction

Figure B.7: Frequency components of the beam error after the step. The red plot shows background frequencies and blue plot shows effect of stage motion on the beam

C

Model parameters

C.1. Mass calculation

Mass for the lumped mass of the system model is calculated in table C.1. And figure C.1 shows various parts of the EOC.

Figure C.1: Electron optical column: Cross section view

Table C.1: Mass calculation

Part Name	Mass (in kg)	# of parts	Total mass (in kg)
m_1			
Damped frame + crane (from CAD)	781.6	1	781.6
Turbo-molecular pump	17	2	34
bottom plate of exposure chamber	88.3	1	88.3
		Total	**903.9**
m_2			
Exposure chamber top plate	207.6	1	207.6
Side plates	46.2	4	184.8
Suspension top plate	68.5	1	68.5
CSR	87	1	87
Other	13.7	1	13.7
		Total	**561.6**
m_3			
Stage assembly	41.4	1	41.4
Suspension (except top plate)	68	1	68
other	1.2	1	1.2
		Total	**110.6**
m_4			
Deflection shroud	7	1	7
BB shroud	7	1	7
C2 shroud	5	1	5
V5 shroud	7	1	7
Aligner shroud	10	1	10
Outer bucket	27	1	27
Inner bucket	13	1	13
Ceramic	5	1	5
igp1 (Ion getter pump 1)	5	1	5
igp2 & igp3	18 & 10	0[1]	0
igp4	5	1	5
Smaller parts	29	1	29
		Total	**120**

C.2. Stiffness calculation

The MaxDamp curve in figure C.2 is the horizontal transmisssibility plot of the air dampers of the EBPG. The dampers' first eigen frequency (f) is ~2 Hz. k_1 is calculated using:

$$k_1 = m_{total}.\omega^2 = 2.6 \times 10^5 \text{N/m}$$

Where, $m_{total} = m_1 + m_2 + m_3 + m_4 = 1648.1kg$ and $\omega = 2\pi f = 12.6rad/s$.

Stiffness k_2 and k_3 are calculated using FEA, by applying incremental force on the part and plotting it against the resulting deflection. The slope of the plot will the stiffness, since $k = Force/deflection$.

For the exposure chamber, the bottom plate is constrained and the force is applied on the top plate in X-direction. Also the gravitational force, the weight of the EOC, and vacuum in the chamber are simulated as shown in figure C.3a.

For the suspension assembly, a simplified CAD is used and the surface near the column opening is constrained. Gravity and weight of stage are applied to the model. And an incremental force is applied on the bottom plate. Figure C.3b depicts the force and constraint on the suspension.

---

[1] In the new EBPG5200, IGP2 and IGP3 are removed.

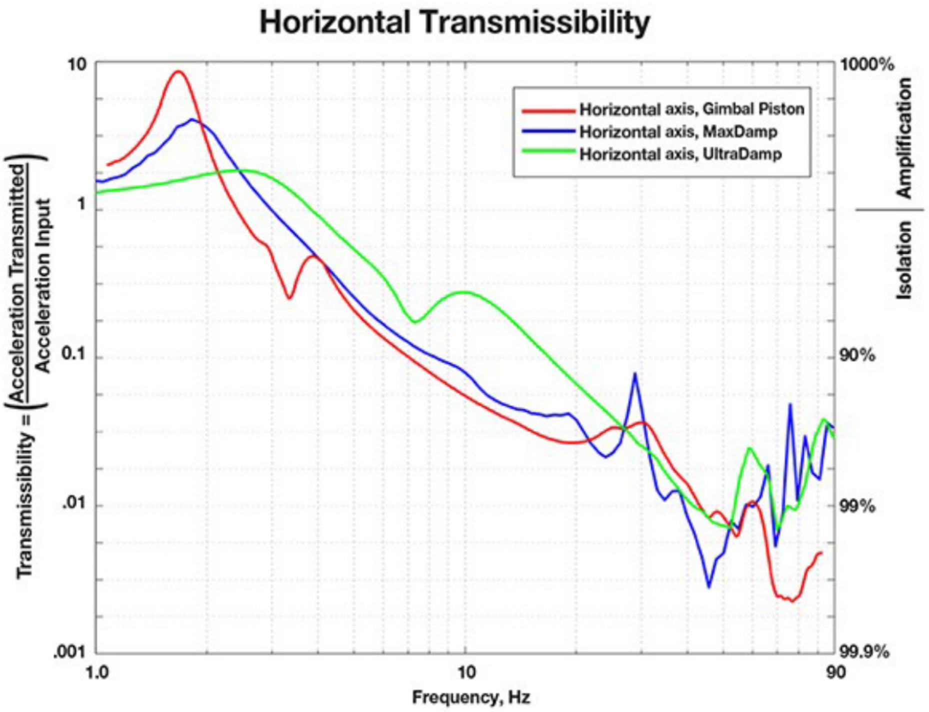

Figure C.2: Transmisibility plots for various air dampers. MaxDamp air dampers are used in the EBPG

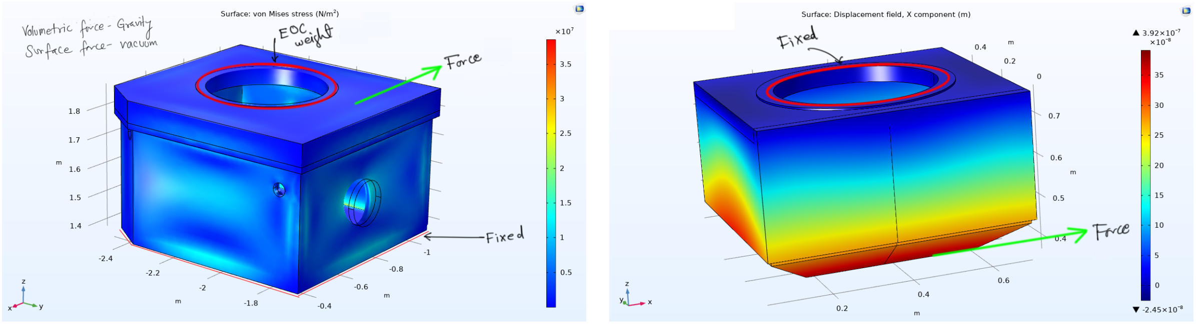

(a) Forces and constraint on Exposure chamber

(b) Forces and constraint on stage suspension

Figure C.3

C.3. Damping coefficient calculation

It can be seen in figure C.2 that the quality factor($Q1$) for the dampers is 6.

The damping ratio of metal structures with joints ($\zeta 2$) is 0.07 and damping ratio of large diameter pipe ($\zeta 4$) is 0.03. The quality factor

$$Q = \frac{1}{2\zeta}$$

Using

$$c = \frac{\sqrt{k \times m_{effective}}}{Q}$$

damping coefficients (c) are calculated.

D

Simulations

D.1. Design iterations of counter mass base plate

D.1.1. Base plate without ribs

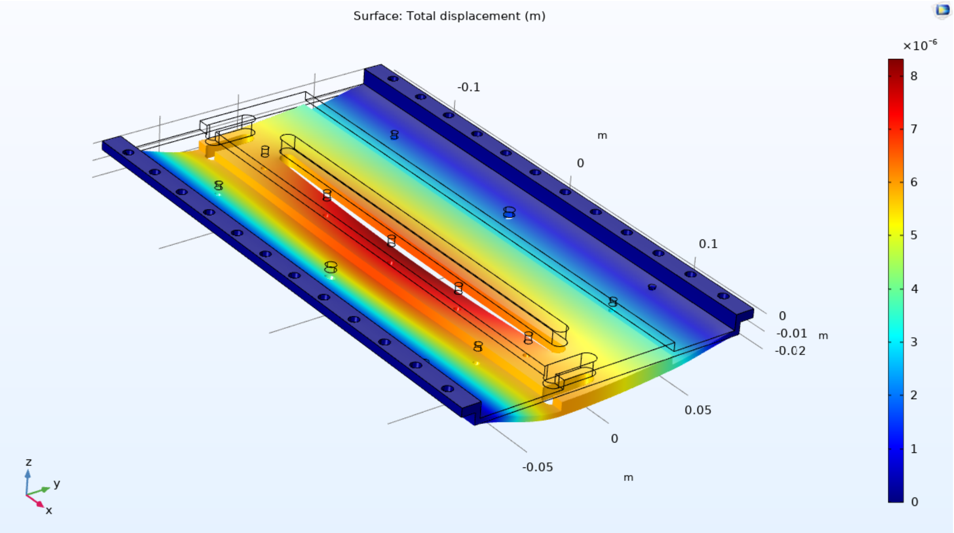

Figure D.1: Deformation plot for the base plate without ribs

D.1.2. Base plate with ribs in the middle and corners

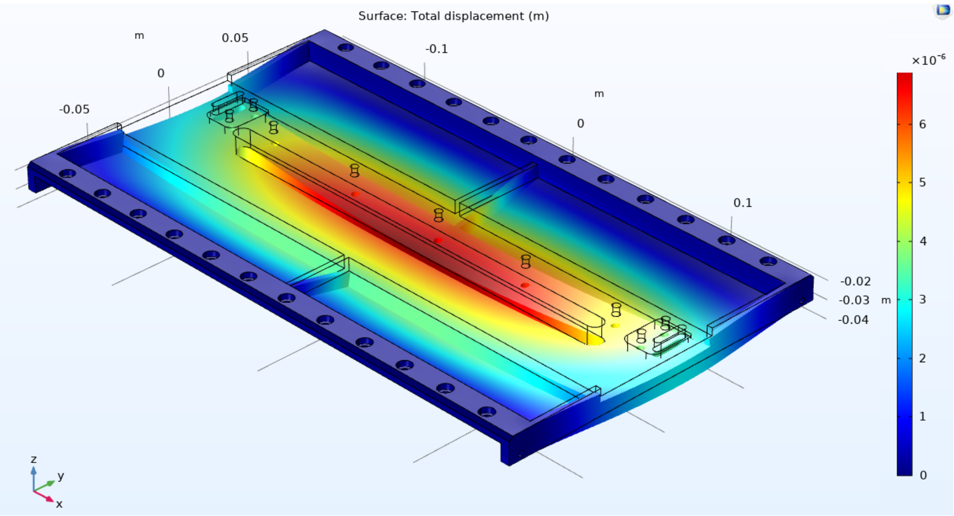

Figure D.2: Deformation plot for the base plate with ribs in the middle and corners

D.1.3. Base plate with ribs in the corners

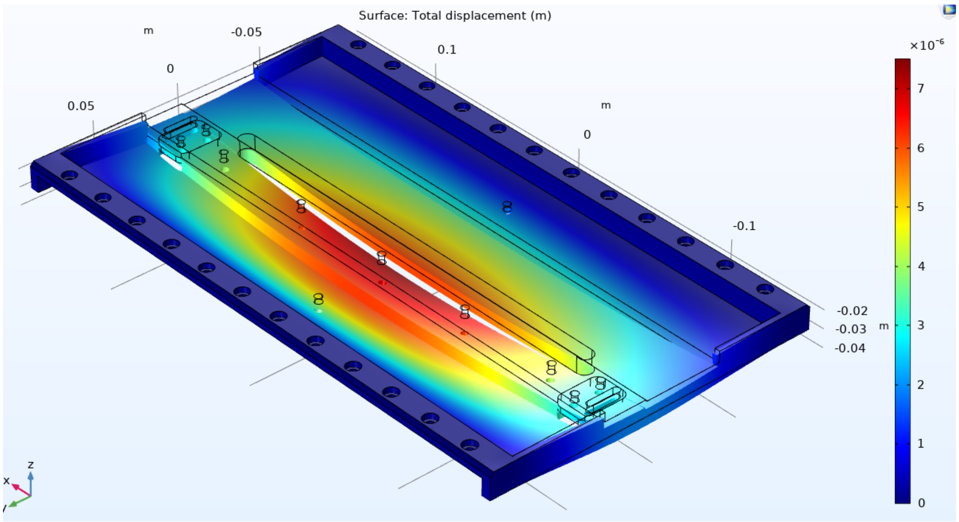

Figure D.3: Deformation plot for the base plate with ribs in the corners

D.2. Simulation of tuned mass damper on the column

The EBPG is modelled for the X-direction motion equipped with a tuned mass damper as shown in figure D.4. And the results of the tuned mass damper on the system dynamics are shown in figure D.5.

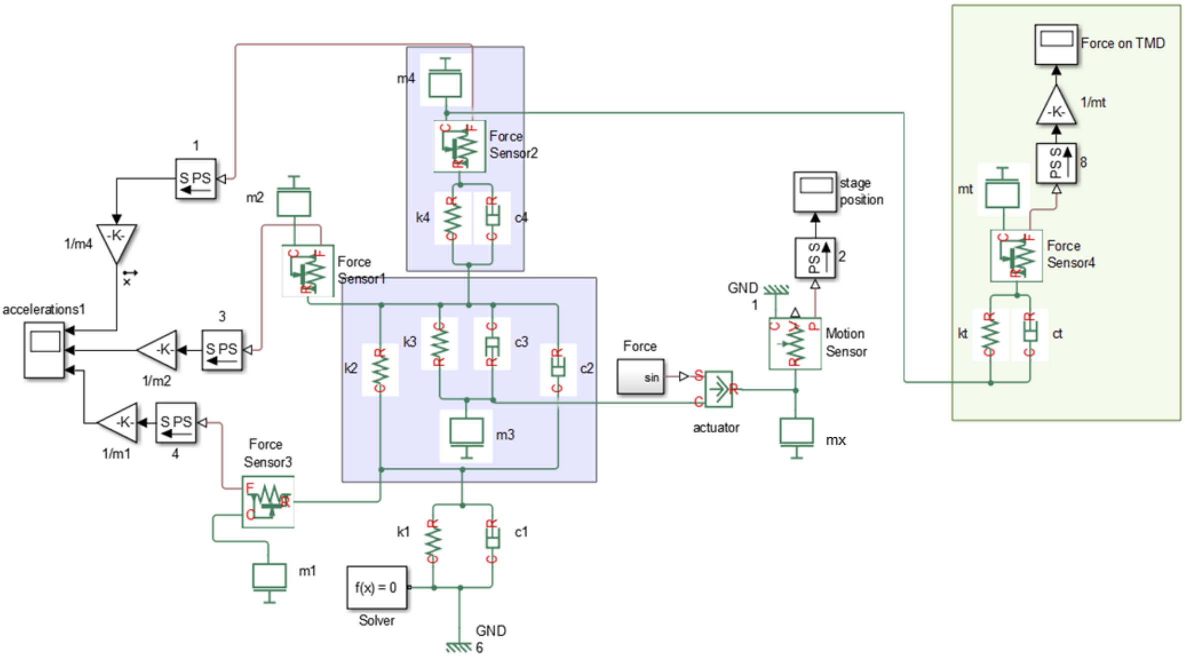

Figure D.4: EPBG model equipped with a tuned mass damper for Y-stage motion

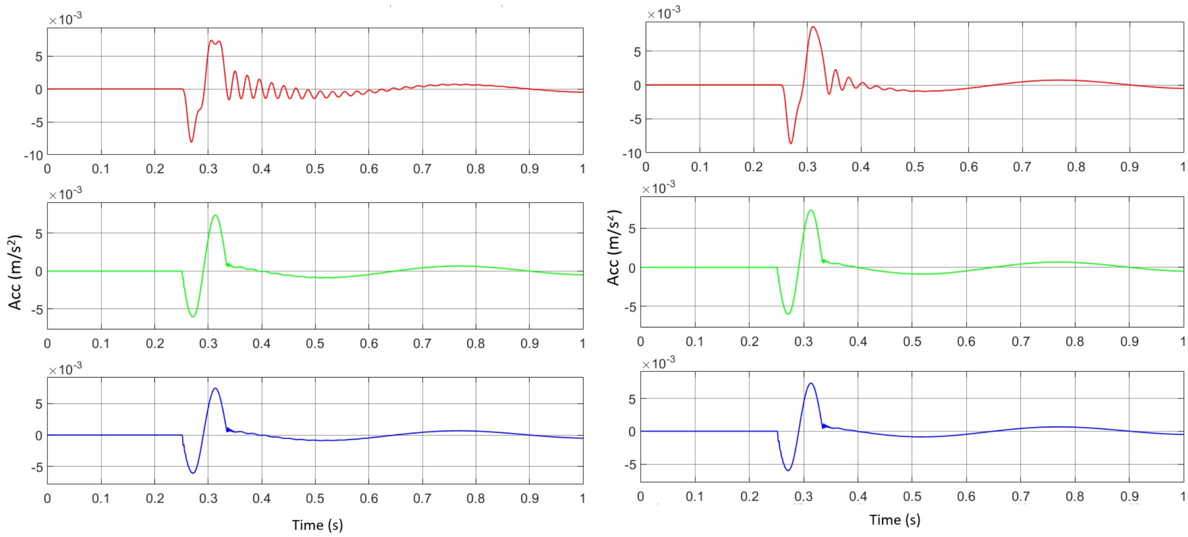

(a)

(b)

Figure D.5: Acceleration vs time plot (a) Current system (b) System equpped with a tuned mass damper

D.3. Friction calculation for the counter mass

The following calculation examines the capability of friction force to avoid slipping of tungsten plates during stage motion.

Friction force,

$$F_r = \mu.\mathrm{N} > 2.94 \times m_{block}$$

Where, μ is the friction coefficient between tungsten and AMC in vacuum (μ>0.3) and N is the normal force by tungsten blocks on the AMC base plate (N> weight of the block i.e. $9.8 \times m_{block}$)

Force due to acceleration,

$$F_a = a_{max}.m_{block} = 1.4 \times m_{block}$$

Where, a_{max} is maximum acceleration of the X-stage i.e. 1.4 m/s^2.

$$F_r > F_a$$

Bibliography

[1] EBPG5200 Pre-Installation Requirements Manual, Raith BV. .

[2] Vistec PG5200 Servo pinion FEA Rev-B, Raith BV. .

[3] The limits of optical lithography. *Principles of Lithography*, page 331–354. doi: 10.1117/3.601520.ch10.

[4] Electron beam lithography. *Nanolithography Techniques*, Jul 2018. URL `http://www.nanolithography.org/2018/07/18/electron-beam-lithography/`.

[5] Consultancy.eu. Global chip shortage costs automotive sector €90 billion. *Consultancy.eu*, May 2021. URL `https://www.consultancy.eu/news/6273/global-chip-shortage-costs-automotive-sector-90-billion`.

[6] Z. Cui. *Nanofabrication: Principles, Capabilities and Limits*. Springer International Publishing, Switzerland, second edition, 2017.

[7] Abdollah Javidialesaadi and Nicholas E. Wierschem. Energy transfer and passive control of single-degree-of-freedom structures using a one-directional rotational inertia viscous damper. *Engineering Structures*, 196:109339, 2019. doi: 10.1016/j.engstruct.2019.109339.

[8] Bas Ketelaars. Internal company report, raith bv. 2021.

[9] Paul Lambrechts, Matthijs Boerlage, and Maarten Steinbuch. Trajectory planning and feedforward design for electromechanical motion systems. *Control Engineering Practice*, 13(2):145–157, 2005. doi: 10.1016/j.conengprac.2004.02.010.

[10] Mark A. Lau and Lucy Y. Pao. Input shaping and time-optimal control of flexible structures. *Automatica*, 39(5):893–900, 2003. doi: 10.1016/s0005-1098(03)00024-4.

[11] Min-Hyun Lee, Hyun-Mi Kim, Seong-Yong Cho, Kipil Lim, Soo-Yeon Park, Jae Jong Lee, and Ki-Bum Kim. Fabrication of ultra-high-density nanodot array patterns (3 tbits/in.2) using electron-beam lithography. *Journal of Vacuum Science Technology B, Nanotechnology and Microelectronics: Materials, Processing, Measurement, and Phenomena*, 29(6):061602, 2011. doi: 10.1116/1.3646469.

[12] Sergio O. Martinez-Chapa, Arnoldo Salazar, and Marc J. Madou. Two-photon polymerization as a component of desktop integrated manufacturing platforms. *Three-Dimensional Microfabrication Using Two-photon Polymerization*, page 374–416, 2016. doi: 10.1016/b978-0-323-35321-2.00019-4.

[13] F Orban. Damping of materials and members in structures. *Journal of Physics: Conference Series*, 268:012022, 2011. doi: 10.1088/1742-6596/268/1/012022.

[14] Reza Rahemi and Dongyang Li. Variation in electron work function with temperature and its effect on the young's modulus of metals. *Scripta Materialia*, 99:41–44, 2015. doi: 10.1016/j.scriptamat.2014.11.022.

[15] Tarunraj Singh and William Singhose. Tutorial on input shaping/time delay control of maneuvering flexible structures.

[16] Tarunraj Singh and Tomas Vyhlidal. Recent results in reference prefiltering for precision motion control. 1994.

[17] Stuart T. Smith and Richard K. Leach. *Basics of precision engineering*. CRC Press Taylor Francis Group, 2018.

[18] S. A. van den Boogaart. Metrology design for improving the beam stability in an e-beam lithography machine. 2020.